

REVIEW ARTICLE

The electronic properties of bilayer graphene

To cite this article: Edward McCann and Mikito Koshino 2013 *Rep. Prog. Phys.* **76** 056503

View the [article online](#) for updates and enhancements.

Related content

- [Electronic properties of graphene: a perspective from scanning tunneling microscopy and magnetotransport](#)
- [Electron-hole asymmetry and energy gaps in bilayer graphene](#)
- [Geometrical and topological aspects of graphene and related materials](#)

Recent citations

- [Shobha Kumbar *et al*](#)
- [Specific stacking angles of bilayer graphene grown on atomic-flat and -stepped Cu surfaces](#)
Hyeyeon Cho *et al*
- [Unconventional reentrant quantum Hall effect in a HgTe/CdHgTe double quantum well](#)
M. V. Yakunin *et al*



IOP | ebooks™

Bringing together innovative digital publishing with leading authors from the global scientific community.

Start exploring the collection—download the first chapter of every title for free.

The electronic properties of bilayer graphene

Edward McCann¹ and Mikito Koshino²

¹ Department of Physics, Lancaster University, Lancaster, LA1 4YB, UK

² Department of Physics, Tohoku University, Sendai, 980-8578, Japan

Received 15 June 2012, in final form 2 January 2013

Published 19 April 2013

Online at stacks.iop.org/RoPP/76/056503

Abstract

We review the electronic properties of bilayer graphene, beginning with a description of the tight-binding model of bilayer graphene and the derivation of the effective Hamiltonian describing massive chiral quasiparticles in two parabolic bands at low energies. We take into account five tight-binding parameters of the Slonczewski–Weiss–McClure model of bulk graphite plus intra- and interlayer asymmetry between atomic sites which induce band gaps in the low-energy spectrum. The Hartree model of screening and band-gap opening due to interlayer asymmetry in the presence of external gates is presented. The tight-binding model is used to describe optical and transport properties including the integer quantum Hall effect, and we also discuss orbital magnetism, phonons and the influence of strain on electronic properties. We conclude with an overview of electronic interaction effects.

(Some figures may appear in colour only in the online journal)

This article was invited by Rolf J Haug.

Contents

1. Introduction	1	3.2. Hartree model of screening	12
2. Electronic band structure	2	4. Transport properties	15
2.1. The crystal structure and the Brillouin zone	2	4.1. Introduction	15
2.2. The tight-binding model	3	4.2. Ballistic transport in a finite system	15
2.3. Effective two-band Hamiltonian at low energies	7	4.3. Transport in disordered bilayer graphene	17
2.4. Interlayer coupling γ_1 : massive chiral electrons	8	5. Optical properties	19
2.5. Interlayer coupling γ_3 : trigonal warping and the Lifshitz transition	8	6. Orbital magnetism	20
2.6. Interlayer coupling γ_4 and on-site parameter Δ' : electron–hole asymmetry	9	7. Phonons and strain	20
2.7. Asymmetry between on-site energies: band gaps	9	7.1. The influence of strain on electrons in bilayer graphene	20
2.8. Next-nearest neighbour hopping	10	7.2. Phonons in bilayer graphene	21
2.9. Spin–orbit coupling	10	7.3. Optical phonon anomaly	22
2.10. The integer quantum Hall effect	10	8. Electronic interactions	23
3. Tuneable band gap	12	9. Summary	24
3.1. Experiments	12	Acknowledgments	24
		References	24

1. Introduction

The production by mechanical exfoliation of isolated flakes of graphene with excellent conducting properties [1] was

soon followed by the observation of an unusual sequence of plateaus in the integer quantum Hall effect in monolayer graphene [2, 3]. This confirmed the fact that charge carriers in monolayer graphene are massless chiral quasiparticles with

a linear dispersion, as described by a Dirac-like effective Hamiltonian [4–6], and it prompted an explosion of interest in the field [7].

The integer quantum Hall effect in bilayer graphene [8] is arguably even more unusual than in monolayer because it indicates the presence of massive chiral quasiparticles [9] with a parabolic dispersion at low energies. The effective Hamiltonian of bilayer graphene may be viewed as a generalization of the Dirac-like Hamiltonian of monolayer graphene and the second (after the monolayer) in a family of chiral Hamiltonians that appear at low energies in *ABC*-stacked (rhombohedral) multilayer graphene [9–15]. In addition to interesting underlying physics, bilayer graphene holds potential for electronics applications, not least because of the possibility to control both carrier density and energy band gap through doping or gating [9, 10, 16–20].

Not surprisingly, many of the properties of bilayer graphene are similar to those in monolayer [7, 21]. These include excellent electrical conductivity with room temperature mobility of up to $40\,000\text{ cm}^2\text{ V}^{-1}\text{ s}^{-1}$ in air [22]; the possibility to tune electrical properties by changing the carrier density through gating or doping [1, 8, 16]; high thermal conductivity with room temperature thermal conductivity of about $2800\text{ W m}^{-1}\text{ K}^{-1}$ [23, 24]; mechanical stiffness, strength and flexibility (Young's modulus is estimated to be about 0.8 TPa [25, 26]); transparency with transmittance of white light of about 95% [27]; impermeability to gases [28]; and the ability to be chemically functionalized [29]. Thus, as with monolayer graphene, bilayer graphene has potential for future applications in many areas [21] including transparent, flexible electrodes for touch screen displays [30]; high-frequency transistors [31]; thermoelectric devices [32]; photonic devices including plasmonic devices [33] and photodetectors [34]; energy applications including batteries [35, 36]; and composite materials [37, 38].

It should be stressed, however, that bilayer graphene has features that make it distinct from monolayer. The low-energy band structure, described in detail in section 2, is different. Like monolayer, intrinsic bilayer has no band gap between its conduction and valence bands, but the low-energy dispersion is quadratic (rather than linear as in monolayer) with massive chiral quasiparticles [8, 9] rather than massless ones. As there are two layers, bilayer graphene represents the thinnest possible limit of an intercalated material [35, 36]. It is possible to address each layer separately leading to entirely new functionalities in bilayer graphene including the possibility to control an energy band gap of up to about 300 meV through doping or gating [9, 10, 16–20]. Recently, this band gap has been used to create devices—constrictions and dots—by electrostatic confinement with gates [39]. Bilayer or multilayer graphene devices may also be preferable to monolayer ones when there is a need to use more material for increased electrical or thermal conduction, strength [37, 38], or optical signature [33].

In the following we review the electronic properties of bilayer graphene. Section 2 is an overview of the electronic tight-binding Hamiltonian and resulting band structure describing the low-energy chiral Hamiltonian and

taking into account different parameters that couple atomic orbitals as well as external factors that may change the electron bands by, for example, opening a band gap. We include the Landau level spectrum in the presence of a perpendicular magnetic field and the corresponding integer quantum Hall effect. In section 3 we consider the opening of a band gap due to doping or gating and present a simple analytical model that describes the density dependence of the band gap by taking into account screening by electrons on the bilayer device. The tight-binding model is used to describe transport properties, section 4, and optical properties, section 5. We also discuss orbital magnetism in section 6, phonons and the influence of strain in section 7. Section 8 concludes with an overview of electronic-interaction effects. Note that this review considers Bernal-stacked (also known as *AB*-stacked) bilayer graphene; we do not consider other stacking types such as *AA*-stacked graphene [40], twisted graphene [41–46] or two graphene sheets separated by a dielectric with, possibly, electronic interactions between them [47–52].

2. Electronic band structure

2.1. The crystal structure and the Brillouin zone

Bilayer graphene consists of two coupled monolayers of carbon atoms, each with a honeycomb crystal structure. Figure 1 shows the crystal structure of monolayer graphene, figure 2 shows bilayer graphene. In both cases, primitive lattice vectors \mathbf{a}_1 and \mathbf{a}_2 may be defined as

$$\mathbf{a}_1 = \left(\frac{a}{2}, \frac{\sqrt{3}a}{2} \right), \quad \mathbf{a}_2 = \left(\frac{a}{2}, -\frac{\sqrt{3}a}{2} \right), \quad (1)$$

where $a = |\mathbf{a}_1| = |\mathbf{a}_2|$ is the lattice constant, the distance between adjacent unit cells, $a = 2.46\text{ Å}$ [53]. Note that the lattice constant is distinct from the carbon–carbon bond length $a_{\text{CC}} = a/\sqrt{3} = 1.42\text{ Å}$, which is the distance between adjacent carbon atoms.

In monolayer graphene, each unit cell contains two carbon atoms, labelled *A* and *B*, figure 1(a). The positions of *A* and *B* atoms are not equivalent because it is not possible to connect them with a lattice vector of the form $\mathbf{R} = n_1\mathbf{a}_1 + n_2\mathbf{a}_2$, where n_1 and n_2 are integers. Bilayer graphene consists of two coupled monolayers, with four atoms in the unit cell, labelled *A1*, *B1* on the lower layer and *A2*, *B2* on the upper layer. The layers are arranged so that one of the atoms from the lower layer *B1* is directly below an atom, *A2*, from the upper layer. We refer to these two atomic sites as ‘dimer’ sites because the electronic orbitals on them are coupled together by a relatively strong interlayer coupling. The other two atoms, *A1* and *B2*, do not have a counterpart on the other layer that is directly above or below them, and are referred to as ‘non-dimer’ sites. Note that some authors [10, 54–56] employ different definitions of *A* and *B* sites as used here. The point group of the bilayer crystal structure is D_{3d} [12, 57, 58] consisting of elements $(\{E, 2C_3, 3C_2', i, 2S_6, 3\sigma_d\})$, and it may be regarded as a direct product of group D_3 $(\{E, 2C_3, 3C_2'\})$ with the inversion group

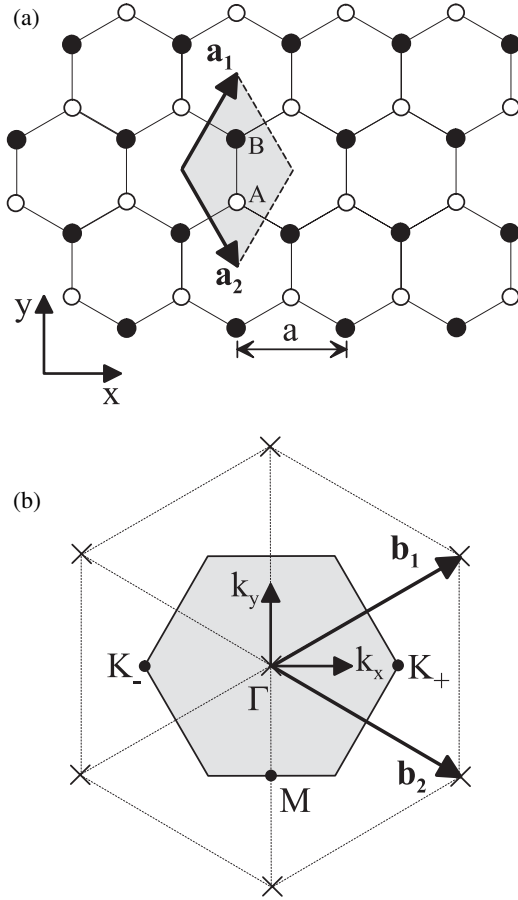


Figure 1. (a) Crystal structure of monolayer graphene with A (B) atoms shown as white (black) circles. The shaded rhombus is the conventional unit cell, \mathbf{a}_1 and \mathbf{a}_2 are primitive lattice vectors. (b) Reciprocal lattice of monolayer and bilayer graphene with lattice points indicated as crosses, \mathbf{b}_1 and \mathbf{b}_2 are primitive reciprocal lattice vectors. The shaded hexagon is the first Brillouin zone with Γ indicating the centre, and K_+ and K_- showing two non-equivalent corners.

C_i ($\{E, i\}$). Thus, the lattice is symmetric with respect to spatial inversion symmetry $(x, y, z) \rightarrow (-x, -y, -z)$.

Primitive reciprocal lattice vectors \mathbf{b}_1 and \mathbf{b}_2 of monolayer and bilayer graphene, where $\mathbf{a}_1 \cdot \mathbf{b}_1 = \mathbf{a}_2 \cdot \mathbf{b}_2 = 2\pi$ and $\mathbf{a}_1 \cdot \mathbf{b}_2 = \mathbf{a}_2 \cdot \mathbf{b}_1 = 0$, are given by

$$\mathbf{b}_1 = \left(\frac{2\pi}{a}, \frac{2\pi}{\sqrt{3}a} \right), \quad \mathbf{b}_2 = \left(\frac{2\pi}{a}, -\frac{2\pi}{\sqrt{3}a} \right). \quad (2)$$

As shown in figure 1(b), the reciprocal lattice is a hexagonal Bravais lattice, and the first Brillouin zone is a hexagon.

2.2. The tight-binding model

2.2.1. An arbitrary crystal structure. In the following, we will describe the tight-binding model [53, 59, 60] and its application to bilayer graphene. We begin by considering an arbitrary crystal with translational invariance and M atomic orbitals ϕ_m per unit cell, labelled by index $m = 1 \dots M$. Bloch states $\Phi_m(\mathbf{k}, \mathbf{r})$ for a given position vector \mathbf{r} and wave vector

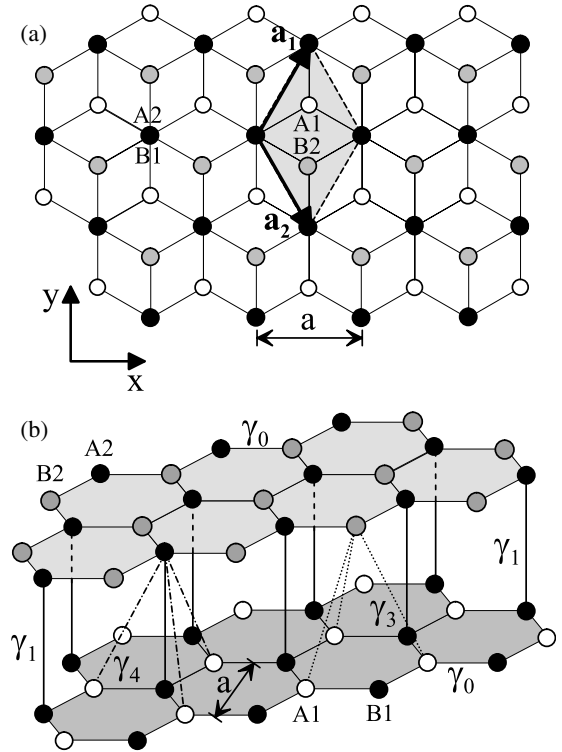


Figure 2. (a) Plan and (b) side view of the crystal structure of bilayer graphene. Atoms A1 and B1 on the lower layer are shown as white and black circles, A2, B2 on the upper layer are black and grey, respectively. The shaded rhombus in (a) indicates the conventional unit cell.

\mathbf{k} may be written as

$$\Phi_m(\mathbf{k}, \mathbf{r}) = \frac{1}{\sqrt{N}} \sum_{i=1}^N e^{i\mathbf{k} \cdot \mathbf{R}_{m,i}} \phi_m(\mathbf{r} - \mathbf{R}_{m,i}), \quad (3)$$

where N is the number of unit cells, $i = 1 \dots N$ labels the unit cell, and $\mathbf{R}_{m,i}$ is the position vector of the m th orbital in the i th unit cell.

The electronic wave function $\Psi_j(\mathbf{k}, \mathbf{r})$ may be expressed as a linear superposition of Bloch states

$$\Psi_j(\mathbf{k}, \mathbf{r}) = \sum_{m=1}^M \psi_{j,m}(\mathbf{k}) \Phi_m(\mathbf{k}, \mathbf{r}), \quad (4)$$

where $\psi_{j,m}$ are expansion coefficients. There are M different energy bands, and the energy $E_j(\mathbf{k})$ of the j th band is given by $E_j(\mathbf{k}) = \langle \Psi_j | \mathcal{H} | \Psi_j \rangle / \langle \Psi_j | \Psi_j \rangle$ where \mathcal{H} is the Hamiltonian. Minimizing the energy E_j with respect to the expansion coefficients $\psi_{j,m}$ [53, 60] leads to

$$H\psi_j = E_j S\psi_j, \quad (5)$$

where ψ_j is a column vector, $\psi_j^T = (\psi_{j1}, \psi_{j2}, \dots, \psi_{jM})$. The transfer integral matrix H and overlap integral matrix S are $M \times M$ matrices with matrix elements defined by

$$H_{mm'} = \langle \Phi_m | \mathcal{H} | \Phi_{m'} \rangle, \quad S_{mm'} = \langle \Phi_m | \Phi_{m'} \rangle. \quad (6)$$

The band energies E_j may be determined from the generalized eigenvalue equation (5) by solving the secular equation

$$\det(H - E_j S) = 0, \quad (7)$$

where ‘det’ stands for the determinant of the matrix.

In order to model a given system in terms of the generalized eigenvalue problem (5), it is necessary to determine the matrices H and S . We will proceed by considering the relatively simple case of monolayer graphene, before generalizing the approach to bilayers. In the following sections, we will omit the subscript j on ψ_j and E_j in equation (5), remembering that the number of solutions is M , the number of orbitals per unit cell.

2.2.2. Monolayer graphene. Here, we will outline how to apply the tight-binding model to graphene, and refer the reader to tutorial-style reviews [53, 60] for further details. We take into account one $2p_z$ orbital per atomic site and, as there are two atoms in the unit cell of monolayer graphene, figure 1(a), we include two orbitals per unit cell labelled as $m = A$ and $m = B$ (the A atoms and the B atoms are each arranged on an hexagonal Bravais lattice).

We begin by considering the diagonal element H_{AA} of the transfer integral matrix H , equation (6), for the A site orbital. It may be determined by substituting the Bloch function (3) for $m = A$ into the matrix element (6), which results in a double sum over the positions of the unit cells in the crystal. Assuming that the dominant contribution arises from those terms involving a given orbital interacting with itself (i.e. in the same unit cell), the matrix element may be written as

$$H_{AA} \approx \frac{1}{N} \sum_{i=1}^N \langle \phi_A(\mathbf{r} - \mathbf{R}_{A,i}) | \mathcal{H} | \phi_A(\mathbf{r} - \mathbf{R}_{A,i}) \rangle. \quad (8)$$

This may be regarded as a summation over all unit cells of a parameter $\epsilon_A = \langle \phi_A(\mathbf{r} - \mathbf{R}_{A,i}) | \mathcal{H} | \phi_A(\mathbf{r} - \mathbf{R}_{A,i}) \rangle$ that takes the same value in every unit cell. Thus, the matrix element may be simply expressed as $H_{AA} \approx \epsilon_A$. Similarly, the diagonal element H_{BB} for the B site orbital can be written as $H_{BB} = \epsilon_B$, while for intrinsic graphene ϵ_A is equal to ϵ_B as the two sublattices are identical. The calculation of the diagonal elements of the overlap integral matrix S , equation (6), proceeds in the same way as that of H , with the overlap of an orbital with itself equal to unity, $\langle \phi_j(\mathbf{r} - \mathbf{R}_{j,i}) | \phi_j(\mathbf{r} - \mathbf{R}_{j,i}) \rangle = 1$. Thus, $S_{BB} = S_{AA} = 1$.

The off-diagonal element H_{AB} of the transfer integral matrix H describes the possibility of hopping between orbitals on A and B sites. Substituting the Bloch function (3) into the matrix element (6) results in a sum over all A sites and a sum over all B sites. We assume that the dominant contribution arises from hopping between adjacent sites. If we consider a given A site, say, then we take into account the possibility of hopping to its three nearest-neighbour B sites, labelled by index $l = 1, 2, 3$:

$$H_{AB} \approx \frac{1}{N} \sum_{i=1}^N \sum_{l=1}^3 e^{ik \cdot \delta_l} \times \langle \phi_A(\mathbf{r} - \mathbf{R}_{A,i}) | \mathcal{H} | \phi_B(\mathbf{r} - \mathbf{R}_{A,i} - \delta_l) \rangle, \quad (9)$$

where δ_l are the positions of three nearest B atoms relative to a given A atom, which may be written as $\delta_1 = (0, a/\sqrt{3})$, $\delta_2 = (a/2, -a/2\sqrt{3})$, $\delta_3 = (-a/2, -a/2\sqrt{3})$.

The sum with respect to the three nearest-neighbour B sites is identical for every A site. A hopping parameter may be defined as

$$\gamma_0 = -\langle \phi_A(\mathbf{r} - \mathbf{R}_{A,i}) | \mathcal{H} | \phi_B(\mathbf{r} - \mathbf{R}_{A,i} - \delta_l) \rangle, \quad (10)$$

which is positive. Then, the matrix element may be written as

$$H_{AB} \approx -\gamma_0 f(\mathbf{k}); \quad f(\mathbf{k}) = \sum_{l=1}^3 e^{ik \cdot \delta_l}, \quad (11)$$

The other off-diagonal matrix element is given by $H_{BA} = H_{AB}^* \approx -\gamma_0 f^*(\mathbf{k})$. The function $f(\mathbf{k})$ describing nearest-neighbour hopping, equation (11), is given by

$$f(\mathbf{k}) = e^{ik_y a/\sqrt{3}} + 2e^{-ik_y a/2\sqrt{3}} \cos(k_x a/2), \quad (12)$$

where $\mathbf{k} = (k_x, k_y)$ is the in-plane wave vector. The calculation of the off-diagonal elements of the overlap integral matrix S is similar to those of H . A parameter $s_0 = \langle \phi_A(\mathbf{r} - \mathbf{R}_{A,i}) | \phi_B(\mathbf{r} - \mathbf{R}_{B,l}) \rangle$ is introduced to describe the possibility of non-zero overlap between orbitals on adjacent sites, giving $S_{AB} = S_{BA}^* = s_0 f(\mathbf{k})$.

Gathering the matrix elements, the transfer H_m and overlap S_m integral matrices of monolayer graphene may be written as

$$H_m = \begin{pmatrix} \epsilon_A & -\gamma_0 f(\mathbf{k}) \\ -\gamma_0 f^*(\mathbf{k}) & \epsilon_B \end{pmatrix}, \quad (13)$$

$$S_m = \begin{pmatrix} 1 & s_0 f(\mathbf{k}) \\ s_0 f^*(\mathbf{k}) & 1 \end{pmatrix}. \quad (14)$$

The corresponding energy may be determined [53] by solving the secular equation (7). For intrinsic graphene, i.e. $\epsilon_A = \epsilon_B = 0$, we have

$$E_{\pm} = \frac{\pm \gamma_0 |f(\mathbf{k})|}{1 \mp s_0 |f(\mathbf{k})|}. \quad (15)$$

The parameter values are listed by Saito *et al* [53] as $\gamma_0 = 3.033$ eV and $s_0 = 0.129$.

The function $f(\mathbf{k})$, equation (12), is zero at the corners of the Brillouin zone, two of which are non-equivalent (i.e. they are not connected by a reciprocal lattice vector). For example, corners K_+ and K_- with wave vectors $\mathbf{K}_{\pm} = \pm(4\pi/3a, 0)$ are labelled in figure 1(b). Such positions are called K points or valleys, and we will use a valley index $\xi = \pm 1$ to distinguish points K_{ξ} . At these positions, the solutions (15) are degenerate, marking a crossing point and zero band gap between the conduction and valence bands. The transfer matrix H_m is approximately equal to a Dirac-like Hamiltonian in the vicinity of the K point, describing massless chiral quasiparticles with a linear dispersion relation. These points are particularly important because the Fermi level is located near them in pristine graphene.

2.2.3. Bilayer graphene. In the tight-binding description of bilayer graphene, we take into account $2p_z$ orbitals on the four atomic sites in the unit cell, labelled as $j = A1, B1, A2, B2$.

Then, the transfer integral matrix of bilayer graphene [9, 10, 54, 61–63] is a 4×4 matrix given by

$$H_b = \begin{pmatrix} \epsilon_{A1} & -\gamma_0 f(\mathbf{k}) & \gamma_4 f(\mathbf{k}) & -\gamma_3 f^*(\mathbf{k}) \\ -\gamma_0 f^*(\mathbf{k}) & \epsilon_{B1} & \gamma_1 & \gamma_4 f(\mathbf{k}) \\ \gamma_4 f^*(\mathbf{k}) & \gamma_1 & \epsilon_{A2} & -\gamma_0 f(\mathbf{k}) \\ -\gamma_3 f(\mathbf{k}) & \gamma_4 f^*(\mathbf{k}) & -\gamma_0 f^*(\mathbf{k}) & \epsilon_{B2} \end{pmatrix}, \quad (16)$$

where the tight-binding parameters are defined as

$$\gamma_0 = -\langle \phi_{A1} | \mathcal{H} | \phi_{B1} \rangle = -\langle \phi_{A2} | \mathcal{H} | \phi_{B2} \rangle, \quad (17)$$

$$\gamma_1 = \langle \phi_{A2} | \mathcal{H} | \phi_{B1} \rangle, \quad (18)$$

$$\gamma_3 = -\langle \phi_{A1} | \mathcal{H} | \phi_{B2} \rangle, \quad (19)$$

$$\gamma_4 = \langle \phi_{A1} | \mathcal{H} | \phi_{A2} \rangle = \langle \phi_{B1} | \mathcal{H} | \phi_{B2} \rangle. \quad (20)$$

Here, we use the notation of the Slonczewski–Weiss–McClure (SWM) model [64–67] that describes bulk graphite. Note that definitions of the parameters used by authors can differ, particularly with respect to signs.

The upper-left and lower-right square 2×2 blocks of H_b describe intralayer terms and are simple generalizations of the monolayer, equation (13). For bilayer graphene, however, we include parameters describing the on-site energies ϵ_{A1} , ϵ_{B1} , ϵ_{A2} , ϵ_{B2} on the four atomic sites, that are not equal in the most general case. As there are four sites, differences between them are described by three parameters [63]:

$$\epsilon_{A1} = \frac{1}{2} (-U + \delta_{AB}), \quad (21)$$

$$\epsilon_{B1} = \frac{1}{2} (-U + 2\Delta' - \delta_{AB}), \quad (22)$$

$$\epsilon_{A2} = \frac{1}{2} (U + 2\Delta' + \delta_{AB}), \quad (23)$$

$$\epsilon_{B2} = \frac{1}{2} (U - \delta_{AB}), \quad (24)$$

where

$$U = \frac{1}{2} [(\epsilon_{A1} + \epsilon_{B1}) - (\epsilon_{A2} + \epsilon_{B2})], \quad (25)$$

$$\Delta' = \frac{1}{2} [(\epsilon_{B1} + \epsilon_{A2}) - (\epsilon_{A1} + \epsilon_{B2})], \quad (26)$$

$$\delta_{AB} = \frac{1}{2} [(\epsilon_{A1} + \epsilon_{A2}) - (\epsilon_{B1} + \epsilon_{B2})]. \quad (27)$$

The three independent parameters are U to describe interlayer asymmetry between the two layers [9, 10, 16–20, 68–74], Δ' for an energy difference between dimer and non-dimer sites [54–56, 67], and δ_{AB} for an energy difference between A and B sites on each layer [63, 75]. These parameters are described in detail in sections 2.6 and 2.7.

The upper-right and lower-left square 2×2 blocks of H_b describe interlayer coupling. Parameter γ_1 describes coupling between pairs of orbitals on the dimer sites $B1$ and $A2$: since this is a vertical coupling, the corresponding terms in H_b (i.e. $H_{A2,B1} = H_{B1,A2} = \gamma_1$) do not contain $f(\mathbf{k})$ which describes in-plane hopping. Parameter γ_3 describes interlayer coupling between non-dimer orbitals $A1$ and $B2$, and γ_4 describes interlayer coupling between dimer and non-dimer orbitals $A1$ and $A2$ or $B1$ and $B2$. Both γ_3 and γ_4 couplings are ‘skew’: they are not strictly vertical, but involve a component of in-plane hopping, and each atom on one layer (e.g. $A1$ for γ_3) has three equidistant nearest-neighbours (e.g. $B2$ for γ_3) on

the other layer. In fact, the in-plane component of this skew hopping is analogous to nearest-neighbour hopping within a single layer, as parametrized by γ_0 . Hence, the skew interlayer hopping (e.g. $H_{A1,B2} = -\gamma_3 f^*(\mathbf{k})$) contains the factor $f(\mathbf{k})$ describing in-plane hopping.

It is possible to introduce an overlap integral matrix for bilayer graphene [63]

$$S_b = \begin{pmatrix} 1 & s_0 f(\mathbf{k}) & 0 & 0 \\ s_0 f^*(\mathbf{k}) & 1 & s_1 & 0 \\ 0 & s_1 & 1 & s_0 f(\mathbf{k}) \\ 0 & 0 & s_0 f^*(\mathbf{k}) & 1 \end{pmatrix}, \quad (28)$$

with a form that mirrors H_b . Here, we only include two parameters: $s_0 = \langle \phi_{A1} | \phi_{B1} \rangle = \langle \phi_{A2} | \phi_{B2} \rangle$ describing non-orthogonality of intralayer nearest-neighbours and $s_1 = \langle \phi_{A2} | \phi_{B1} \rangle$ describing non-orthogonality of orbitals on dimer sites $A1$ and $B2$. In principle, it is possible to introduce additional parameters analogous to γ_3 , γ_4 , etc, but generally they will be small and irrelevant. In fact, it is a common practice to neglect the overlap integral matrix entirely, i.e. replace S_b with a unit matrix, because the influence of parameters s_0 and s_1 describing non-orthogonality of adjacent orbitals is small at low energies $|E| \leq \gamma_1$. Then, the generalized eigenvalue equation (5) reduces to an eigenvalue equation $H_b \psi = E \psi$ with Hamiltonian H_b , equation (16).

The energy differences U and δ_{AB} are usually attributed to extrinsic factors such as gates, substrates or doping. Thus, there are five independent parameters in the Hamiltonian (16) of intrinsic bilayer graphene, namely γ_0 , γ_1 , γ_3 , γ_4 and Δ' . The band structure predicted by the tight-binding model has been compared with observations from photoemission [16], Raman [76] and infrared spectroscopy [55, 56, 78–81]. Parameter values determined by fitting to experiments are listed in table 1 for bulk graphite [67], for bilayer graphene by Raman [76, 77] and infrared [55, 56, 80] spectroscopy, and for Bernal-stacked trilayer graphene by observation of Landau level crossings [82]. Note that there are seven parameters in the SWM model of graphite [64–67] because the next-nearest layer couplings γ_2 and γ_5 , absent in bilayer, are present in graphite (and trilayer graphene, also). Parameter Δ in the SWM model is related by $\Delta = \Delta' + \gamma_2 - \gamma_5$ to the parameter Δ' describing the energy difference between dimer and non-dimer sites in bilayer graphene.

The energy bands are plotted in figure 3 along the k_x axis in reciprocal space intersecting the corners K_- , K_+ and the centre Γ of the Brillouin zone (see figure 1(b)). Plots were made using Hamiltonian H_b , equation (16), with parameter values determined by infrared spectroscopy $\gamma_0 = 3.16$ eV, $\gamma_1 = 0.381$ eV, $\gamma_3 = 0.38$ eV, $\gamma_4 = 0.14$ eV, $\epsilon_{B1} = \epsilon_{A2} = \Delta' = 0.022$ eV, and $\epsilon_{A1} = \epsilon_{B2} = U = \delta_{AB} = 0$ [80]. There are four bands because the model takes into account one $2p_z$ orbital on each of the four atomic sites in the unit cell; a pair of conduction bands and a pair of valence bands. Over most of the Brillouin zone, each pair is split by an energy of the order of the interlayer spacing $\gamma_1 \approx 0.4$ eV [83]. Near the K points, inset of figure 3, one conduction band and one valence band are split away from zero energy by an energy of the order of the interlayer coupling γ_1 , whereas two bands touch at zero

Table 1. Values (in eV) of the SWM model parameters [64–67] determined experimentally. Numbers in parentheses indicate estimated accuracy of the final digit(s). The energy difference between dimer and non-dimer sites in the bilayer is $\Delta' = \Delta - \gamma_2 + \gamma_5$. Note that next-nearest layer parameters γ_2 and γ_5 are not present in bilayer graphene.

Parameter	Graphite [67]	Bilayer [76]	Bilayer [55]	Bilayer [56]	Bilayer [80]	Trilayer [82]
γ_0	3.16(5)	2.9	3.0 ^a	—	3.16(3)	3.1 ^a
γ_1	0.39(1)	0.30	0.40(1)	0.404(10)	0.381(3)	0.39 ^a
γ_2	−0.020(2)	—	—	—	—	−0.028(4)
γ_3	0.315(15)	0.10	0.3 ^a	—	0.38(6)	0.315 ^a
γ_4	0.044(24)	0.12	0.15(4)	—	0.14(3)	0.041(10)
γ_5	0.038(5)	—	—	—	—	0.05(2)
Δ	−0.008(2)	—	0.018(3)	0.018(2)	0.022(3)	−0.03(2)
Δ'	0.050(6)	—	0.018(3)	0.018(2)	0.022(3)	0.046(10)

^a This parameter was not determined by the given experiment, the value quoted was taken from previous literature.

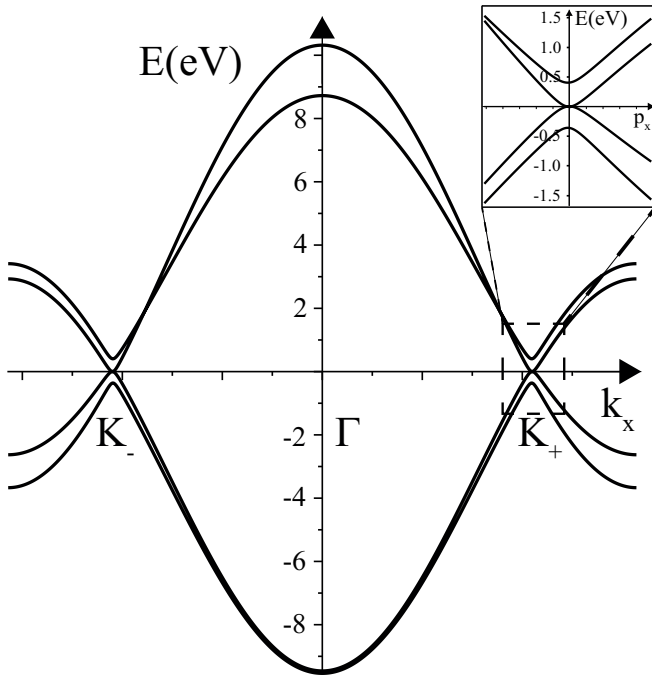


Figure 3. Low-energy bands of bilayer graphene arising from $2p_z$ orbitals plotted along the k_x axis in reciprocal space intersecting the corners K_- , K_+ and the centre Γ of the Brillouin zone. The inset shows the bands in the vicinity of the K_+ point. Plots were made using Hamiltonian H_b , equation (16), with parameter values $\gamma_0 = 3.16$ eV, $\gamma_1 = 0.381$ eV, $\gamma_3 = 0.38$ eV, $\gamma_4 = 0.14$ eV, $\epsilon_{B1} = \epsilon_{A2} = \Delta' = 0.022$ eV, and $\epsilon_{A1} = \epsilon_{B2} = U = \delta_{AB} = 0$ [80].

energy [9]. The ‘split’ bands are a bonding and anti-bonding pair arising from the strong coupling (by interlayer coupling γ_1) of the orbitals on the dimer $B1$ and $A2$ sites, whereas the ‘low-energy’ bands arise from hopping between the non-dimer $A1$ and $B2$ sites. In pristine bilayer graphene, the Fermi level lies at the point where the two low-energy bands touch (shown as zero energy in figure 3) and, thus, this region is relevant for the study of electronic properties. It will be the focus of the following sections.

At low energies, the shape of the band structure predicted by the tight-binding model (see inset in figure 3) is in good agreement with that calculated by density-functional theory [18, 57, 68] and it is possible to obtain values for the tight-binding parameters in this way, generally in line with the

experimental ones listed in table 1. The tight-binding model Hamiltonian H_b , equation (16), used in conjunction with the parameters listed in table 1, is not accurate over the whole Brillouin zone because the fitting of tight-binding parameters is generally carried out in the vicinity of the corners of the Brillouin zone K_+ and K_- (as the Fermi level lies near zero energy). For example, parameter s_0 in equation (28) describing non-orthogonality of adjacent orbitals has been neglected here, but it contributes electron–hole asymmetry which is particularly prevalent near the Γ point at the centre of the Brillouin zone [53, 60].

2.2.4. Effective four-band Hamiltonian near the K points. To describe the properties of electrons in the vicinity of the K points, a momentum $\mathbf{p} = \hbar\mathbf{k} - \hbar\mathbf{K}_\xi$ is introduced which is measured from the centre of the K_ξ point. Expanding in powers of \mathbf{p} , the function $f(\mathbf{k})$, equation (12), is approximately given by $f(\mathbf{k}) \approx -\sqrt{3}a(\xi p_x - ip_y)/2\hbar$ which is valid close to the K_ξ point, i.e. for $pa/\hbar \ll 1$, where $p = |\mathbf{p}| = (p_x^2 + p_y^2)^{1/2}$. In monolayer graphene, the Hamiltonian matrix (13) is simplified by keeping only linear terms in momentum p as

$$H_m = \begin{pmatrix} \epsilon_A & v\pi^\dagger \\ v\pi & \epsilon_B \end{pmatrix}, \quad (29)$$

where $\pi = \xi p_x + ip_y$, $\pi^\dagger = \xi p_x - ip_y$ and $v = \sqrt{3}a\gamma_0/2\hbar$ is the band velocity. In the intrinsic case, $\epsilon_A = \epsilon_B = 0$, the eigenenergy becomes $E = \pm v|\mathbf{p}|$, which approximates equation (15). In bilayer graphene, similarly, equation (16) is reduced to

$$H_b = \begin{pmatrix} \epsilon_{A1} & v\pi^\dagger & -v_4\pi^\dagger & v_3\pi \\ v\pi & \epsilon_{B1} & \gamma_1 & -v_4\pi^\dagger \\ -v_4\pi & \gamma_1 & \epsilon_{A2} & v\pi^\dagger \\ v_3\pi^\dagger & -v_4\pi & v\pi & \epsilon_{B2} \end{pmatrix}, \quad (30)$$

where we introduced the effective velocities, $v_3 = \sqrt{3}a\gamma_3/2\hbar$ and $v_4 = \sqrt{3}a\gamma_4/2\hbar$.

At zero magnetic field Hamiltonian (30) yields four valley-degenerate bands $E(\mathbf{p})$. A simple analytic solution may be obtained by neglecting the terms $v_4\pi$, $v_4\pi^\dagger$ proportional to γ_4 , and by considering only interlayer asymmetry U in the on-site energies: $\epsilon_{A1} = \epsilon_{B1} = -U/2$ and $\epsilon_{A2} = \epsilon_{B2} = U/2$. Then,

there is electron–hole symmetry, i.e. energies may be written $E = \pm \varepsilon_\alpha(\mathbf{p})$, $\alpha = 1, 2$, [9] with

$$\varepsilon_\alpha^2 = \frac{\gamma_1^2}{2} + \frac{U^2}{4} + \left(v^2 + \frac{v_3^2}{2}\right) p^2 + (-1)^\alpha \sqrt{\Gamma}, \quad (31)$$

$$\Gamma = \frac{1}{4} (\gamma_1^2 - v_3^2 p^2)^2 + v^2 p^2 [\gamma_1^2 + U^2 + v_3^2 p^2] + 2\xi \gamma_1 v_3 v^2 p^3 \cos 3\varphi,$$

where φ is the polar angle of momentum $\mathbf{p} = (p_x, p_y) = p(\cos \varphi, \sin \varphi)$. Energy ε_2 describes the higher energy bands split from zero energy by the interlayer coupling γ_1 between the orbitals on the dimer sites $B1, A2$.

Low-energy bands $E = \pm \varepsilon_1$ are related to orbitals on the non-dimer sites $A1, B2$. In an intermediate energy range $U, (v_3/v)^2 \gamma_1 < \varepsilon_1 < \gamma_1$ it is possible to neglect the interlayer asymmetry U and terms proportional to γ_3 (i.e. set $U = v_3 = 0$), and the low-energy bands may be approximated [9] as

$$\varepsilon_1 \approx \frac{1}{2} \gamma_1 \left[\sqrt{1 + 4v^2 p^2 / \gamma_1^2} - 1 \right], \quad (32)$$

which interpolates between an approximately linear dispersion $\varepsilon_1 \approx vp$ at large momentum to a quadratic one $\varepsilon_1 \approx p^2/2m$ at small momentum, where the mass is $m = \gamma_1/2v^2$ (see inset in figure 3). This crossover occurs at $p \approx \gamma_1/2v$. A convenient way to describe the bilayer at low energy and momentum $p \ll \gamma_1/2v$ is to eliminate the components in the Hamiltonian (30) related to the orbitals on dimer sites $B1, A2$, resulting in an effective two-component Hamiltonian describing the orbitals on the non-dimer sites $A1, B2$, and, thus, the two bands that approach each other at zero energy. This is described in the next section, and the solutions of this Hamiltonian are shown to be massive chiral quasiparticles [8, 9], as opposed to massless chiral ones in monolayer graphene.

2.3. Effective two-band Hamiltonian at low energies

In this section we focus on the low-energy electronic band structure in the vicinity of the points K_+ and K_- at the corners of the first Brillouin zone, relevant for energies near the Fermi level. A simple model may be obtained by eliminating orbitals related to the dimer sites, resulting in an effective Hamiltonian for the low-energy orbitals. First, we outline the procedure in general terms, because it may be applied to systems other than bilayer graphene such as ABC -stacked (rhombohedral) graphene multilayers [84, 85], before applying it specifically to bilayer graphene.

2.3.1. General procedure. We consider the energy eigenvalue equation, and consider separate blocks in the Hamiltonian corresponding to low-energy $\theta = (\psi_{A1}, \psi_{B2})^T$ and dimer $\chi = (\psi_{A2}, \psi_{B1})^T$ components:

$$\begin{pmatrix} h_\theta & u \\ u^\dagger & h_\chi \end{pmatrix} \begin{pmatrix} \theta \\ \chi \end{pmatrix} = E \begin{pmatrix} \theta \\ \chi \end{pmatrix}. \quad (33)$$

The second row of (33) allows the dimer components to be expressed in terms of the low-energy ones:

$$\chi = (E - h_\chi)^{-1} u^\dagger \theta. \quad (34)$$

Substituting this into the first row of (33) gives an effective eigenvalue equation written solely for the low-energy components:

$$\begin{aligned} [h_\theta + u(E - h_\chi)^{-1} u^\dagger] \theta &= E\theta, \\ [h_\theta - u h_\chi^{-1} u^\dagger] \theta &\approx ES\theta, \end{aligned}$$

where $S = 1 + u h_\chi^{-2} u^\dagger$. The second equation is accurate up to linear terms in E . Finally, we perform a transformation $\Phi = S^{1/2} \theta$:

$$\begin{aligned} [h_\theta - u h_\chi^{-1} u^\dagger] S^{-1/2} \Phi &\approx ES^{1/2} \Phi, \\ S^{-1/2} [h_\theta - u h_\chi^{-1} u^\dagger] S^{-1/2} \Phi &\approx E\Phi. \end{aligned} \quad (35)$$

This transformation ensures that normalization of Φ is consistent with that of the original states:

$$\begin{aligned} \Phi^\dagger \Phi &= \theta^\dagger S \theta = \theta^\dagger (1 + u h_\chi^{-2} u^\dagger) \theta, \\ &\approx \theta^\dagger \theta + \chi^\dagger \chi, \end{aligned}$$

where we used equation (34) for small E : $\chi \approx -h_\chi^{-1} u^\dagger \theta$. Thus, the effective Hamiltonian for low-energy components is given by equation (35):

$$H^{(\text{eff})} \approx S^{-1/2} [h_\theta - u h_\chi^{-1} u^\dagger] S^{-1/2}, \quad (36)$$

$$S = 1 + u h_\chi^{-2} u^\dagger. \quad (37)$$

2.3.2. Bilayer graphene. The Hamiltonian (30) is written in basis $A1, B1, A2, B2$. If, instead, it is written in the basis of low-energy and dimer components $(\theta, \chi) \equiv A1, B2, A2, B1$, equation (33), then

$$\begin{aligned} h_\theta &= \begin{pmatrix} \epsilon_{A1} & v_3 \pi \\ v_3 \pi^\dagger & \epsilon_{B2} \end{pmatrix}, & h_\chi &= \begin{pmatrix} \epsilon_{A2} & \gamma_1 \\ \gamma_1 & \epsilon_{B1} \end{pmatrix}, \\ u &= \begin{pmatrix} -v_4 \pi^\dagger & v \pi^\dagger \\ v \pi & -v_4 \pi \end{pmatrix}, & u^\dagger &= \begin{pmatrix} -v_4 \pi & v \pi^\dagger \\ v \pi & -v_4 \pi^\dagger \end{pmatrix}. \end{aligned}$$

Using the procedure described in the previous section, equations (36) and (37), it is possible to obtain an effective Hamiltonian $H^{(\text{eff})} \equiv \hat{H}_2$ for components (ψ_{A1}, ψ_{B2}) . An expansion is performed by assuming that the intralayer hopping γ_0 and the interlayer coupling γ_1 are larger than other energies: $\gamma_0, \gamma_1 \gg |E|, vp, |\gamma_3|, |\gamma_4|, |U|, |\Delta'|, |\delta_{AB}|$. Then, keeping only terms that are linear in the small parameters $|\gamma_3|, |\gamma_4|, |U|, |\Delta'|, |\delta_{AB}|$ and quadratic in momentum, the effective Hamiltonian [9, 63] is

$$\begin{aligned} \hat{H}_2 &= \hat{h}_0 + \hat{h}_w + \hat{h}_4 + \hat{h}_\Delta + \hat{h}_U + \hat{h}_{AB}, \\ \hat{h}_0 &= -\frac{1}{2m} \begin{pmatrix} 0 & (\pi^\dagger)^2 \\ \pi^2 & 0 \end{pmatrix}, \\ \hat{h}_w &= v_3 \begin{pmatrix} 0 & \pi \\ \pi^\dagger & 0 \end{pmatrix} - \frac{v_3 a}{4\sqrt{3}\hbar} \begin{pmatrix} 0 & (\pi^\dagger)^2 \\ \pi^2 & 0 \end{pmatrix}, \\ \hat{h}_4 &= \frac{2vv_4}{\gamma_1} \begin{pmatrix} \pi^\dagger \pi & 0 \\ 0 & \pi \pi^\dagger \end{pmatrix}, \end{aligned} \quad (38)$$

$$\begin{aligned}\hat{h}_\Delta &= \frac{\Delta' v^2}{\gamma_1^2} \begin{pmatrix} \pi^\dagger \pi & 0 \\ 0 & \pi \pi^\dagger \end{pmatrix}, \\ \hat{h}_U &= -\frac{U}{2} \left[\begin{pmatrix} 1 & 0 \\ 0 & -1 \end{pmatrix} - \frac{2v^2}{\gamma_1^2} \begin{pmatrix} \pi^\dagger \pi & 0 \\ 0 & -\pi \pi^\dagger \end{pmatrix} \right], \\ \hat{h}_{AB} &= \frac{\delta_{AB}}{2} \begin{pmatrix} 1 & 0 \\ 0 & -1 \end{pmatrix},\end{aligned}$$

where $\pi = \xi p_x + i p_y$, $\pi^\dagger = \xi p_x - i p_y$. In the following sections, we discuss the terms in \hat{H}_2 . The first term \hat{h}_0 describes massive chiral electrons, section 2.4. It generally dominates at low energies $|E| \ll \gamma_1$, so that the other terms in \hat{H}_2 may be considered as perturbations of it. The second term \hat{h}_w , section 2.5, introduces a triangular distortion of the Fermi circle around each K point known as ‘trigonal warping’. Terms \hat{h}_U and \hat{h}_{AB} , with ± 1 on the diagonal, produce a band gap between the conduction and valence bands, section 2.7, whereas \hat{h}_4 and \hat{h}_Δ introduce electron–hole asymmetry into the band structure, section 2.6.

The Hamiltonian (38) is written in the vicinity of a valley with index $\xi = \pm 1$ distinguishing between K_+ and K_- . In order to briefly discuss the effect of symmetry operations on it, we introduce Pauli spin matrices $\sigma_x, \sigma_y, \sigma_z$ in the $A1/B2$ sublattice space and Π_x, Π_y, Π_z in the valley space. Then, the first term in the Hamiltonian may be written as $\hat{h}_0 = -(1/2m)[\sigma_x(p_x^2 - p_y^2) + 2\Pi_z \sigma_y p_x p_y]$. The operation of spatial inversion i is represented by $\Pi_x \sigma_x$ because it swaps both valleys and lattice sites, time inversion is given by complex conjugation and Π_x , as it also swaps valleys. Hamiltonian (38) satisfies time-inversion symmetry at zero magnetic field. The intrinsic terms $\hat{h}_0, \hat{h}_w, \hat{h}_4$ and \hat{h}_Δ satisfy spatial-inversion symmetry because the bilayer crystal structure is spatial-inversion symmetric, but terms \hat{h}_U and \hat{h}_{AB} , with ± 1 on the diagonal, are imposed by external fields and they violate spatial-inversion symmetry, producing a band gap between the conduction and valence bands.

2.4. Interlayer coupling γ_1 : massive chiral electrons

The Hamiltonian \hat{h}_0 in equation (38) resembles the Dirac-like Hamiltonian of monolayer graphene, but with a quadratic-in-momentum term on the off-diagonal rather than linear. For example, the term $\pi^2/2m$ accounts for an effective hopping between the non-dimer sites $A1, B2$ via the dimer sites $B1, A2$ consisting of a hop from $A1$ to $B1$ (contributing a factor $v\pi$), followed by a transition between $B1, A2$ dimer sites (giving a ‘mass’ $\sim \gamma_1$), and a hop from $A2$ to $B2$ (a second factor of $v\pi$). The solutions are massive chiral electrons [8, 9], with parabolic dispersion $E = \pm p^2/2m$, $m = \gamma_1/2v^2$. The density of states is $m/(2\pi\hbar^2)$ per spin and per valley, and the Fermi velocity $v_F = p_F/m$ is momentum dependent, unlike the Fermi velocity v of monolayer graphene.

The corresponding wave function is given by

$$\psi = \frac{1}{\sqrt{2}} \begin{pmatrix} 1 \\ \mp e^{2i\xi\varphi} \end{pmatrix} e^{ip \cdot r/\hbar}. \quad (39)$$

The wave function components describe the electronic amplitudes on the $A1$ and $B2$ sites, and it can be useful

to introduce the concept of a pseudospin degree of freedom [8, 9] that is related to these amplitudes. If all the electronic densities were located on the $A1$ sites, then the pseudospin part of the wave function $|\uparrow\rangle = (1, 0)$ could be viewed as a pseudospin ‘up’ state, pointing upwards out of the graphene plane. Likewise, a state $|\downarrow\rangle = (0, 1)$ with density solely on the $B2$ sites could be viewed as a pseudospin ‘down’ state. However, density is usually shared equally between the two layers, so that the pseudospin is a linear combination of up and down, $|\uparrow\rangle \mp e^{2i\xi\varphi} |\downarrow\rangle$, equation (39), and it lies in the graphene plane.

The Hamiltonian may also be written as $\hat{h}_0 = (p^2/2m) \sigma \cdot \hat{n}_2$ where the pseudospin vector is $\sigma = (\sigma_x, \sigma_y, \sigma_z)$, and $\hat{n}_2 = -(\cos 2\varphi, \xi \sin 2\varphi, 0)$ is a unit vector. This illustrates the chiral nature of the electrons [8, 9]: the chiral operator $\sigma \cdot \hat{n}_2$ projects the pseudospin onto the direction of quantization \hat{n}_2 , which is fixed to lie in the graphene plane, but turns twice as quickly as the momentum p . For these chiral quasiparticles, adiabatic propagation along a closed orbit produces a Berry’s phase [86] change of 2π [8, 9] of the wave function, in contrast to Berry phase π in monolayer graphene.

Note that the chiral Hamiltonian \hat{h}_0 may be viewed as a generalization of the Dirac-like Hamiltonian of monolayer graphene and the second (after the monolayer) in a family of chiral Hamiltonians H_J , $J = 1, 2, \dots$, corresponding to Berry’s phase $J\pi$ which appear at a low energy in ABC -stacked (rhombohedral) multilayer graphene [9–15, 84, 85]:

$$H_J = g_J \begin{pmatrix} 0 & (\pi^\dagger)^J \\ \pi^J & 0 \end{pmatrix}, \quad (40)$$

where $g_1 = v$ for monolayer, $g_2 = -1/2m$ for bilayer and $g_3 = v^3/\gamma_1^2$ for trilayer graphene. Since the pseudospin is related to the wavefunction amplitude on sites that are located on different layers, pseudospin may be viewed as a ‘which layer’ degree of freedom [14, 87].

2.5. Interlayer coupling γ_3 : trigonal warping and the Lifshitz transition

The Hamiltonian \hat{h}_0 in equation (38) yields a quadratic, isotropic dispersion relation $E = \pm p^2/2m$ with circular iso-energetic lines, i.e. there is a circular Fermi line around each K point. This is valid near the K point, $pa/\hbar \ll 1$, whereas, at high energies, and momentum p far from the K point, there is a triangular perturbation of the circular iso-energetic lines known as trigonal warping, as in monolayer graphene and graphite. It occurs because the band structure follows the symmetry of the crystal lattice as described by the full momentum dependence of the function $f(k)$, equation (12) [88].

In bilayer graphene [9], as in bulk graphite [89–92], a second source of trigonal warping arises from the skew interlayer coupling γ_3 between non-dimer $A1$ and $B2$ sites. The influence of γ_3 on the band structure is described by equation (31). In the two-band Hamiltonian, it is described by \hat{h}_w in equation (38), the second term of which arises from a quadratic term in the expansion of $f(k) \approx -\sqrt{3}a(\xi p_x - i p_y)/2\hbar + a^2(\xi p_x + i p_y)^2/8\hbar^2$. This second term has the

same momentum dependence as \hat{h}_0 , and, thus, it actually only gives a small additional contribution to the mass m . The first term in \hat{h}_w causes trigonal warping of the iso-energetic lines in directions $\varphi = \varphi_0$, where $\varphi_0 = 0, \frac{2}{3}\pi, \frac{4}{3}\pi$ at K_+ , $\varphi_0 = \frac{1}{3}\pi, \pi, \frac{5}{3}\pi$ at K_- .

To analyse the influence of \hat{h}_w at low energies, we consider just \hat{h}_0 and the first term in \hat{h}_w , and the resulting energy $E = \pm \varepsilon_1$ is given by

$$\varepsilon_1^2 = (v_3 p)^2 - \frac{\xi v_3 p^3}{m} \cos(3\varphi) + \left(\frac{p^2}{2m}\right)^2, \quad (41)$$

in agreement with equation (31) for $U = 0$, $vp/\gamma_1 \ll 1$ and $v_3/v \ll 1$. As it is linear in momentum, the influence of \hat{h}_w and the resulting triangular distortion of iso-energetic lines tend to increase as the energy and momentum are decreased until a Lifshitz transition [93] occurs at energy

$$\varepsilon_L = \frac{\gamma_1}{4} \left(\frac{v_3}{v}\right)^2 \approx 1 \text{ meV}. \quad (42)$$

For energies $|E| < \varepsilon_L$, iso-energetic lines are broken into four separate ‘pockets’ consisting of one central pocket and three ‘leg’ pockets, the latter centred at momentum $p \approx \gamma_1 v_3/v^2$ and angle φ_0 , as shown in figure 4. The central pocket is approximately circular for $|E| \ll \varepsilon_L$ with area $\mathcal{A}_c \approx \pi \varepsilon^2/(\hbar v_3)^2$, while each leg pocket is approximately elliptical with area $\mathcal{A}_l \approx \mathcal{A}_c/3$. Note that Berry phase 2π is conserved through the Lifshitz transition; the three leg pockets each have Berry phase π while the central pocket has $-\pi$ [12, 94].

2.6. Interlayer coupling γ_4 and on-site parameter Δ' : electron-hole asymmetry

Skew interlayer coupling γ_4 between a non-dimer and a dimer site, i.e. between $A1$ and $A2$ sites or between $B1$ and $B2$ sites, is described by \hat{h}_4 in equation (38), where the effective velocity is $v_4 = \sqrt{3}a\gamma_4/2\hbar$. This term produces electron-hole asymmetry in the band structure, as illustrated by considering the energy eigenvalues $E = \pm(p^2/2m)(1 \pm 2v_4/v)$ of the Hamiltonian $\hat{h}_0 + \hat{h}_4$. The energy difference Δ' between dimer and non-dimer sites, $\epsilon_{A1} = \epsilon_{B2} = 0$, $\epsilon_{B1} = \epsilon_{A2} = \Delta'$, equation (26), also introduces electron-hole asymmetry into the band structure: the low-energy bands described by $\hat{h}_0 + \hat{h}_\Delta$ are given by $E = \pm p^2/2m(1 \pm \Delta'/\gamma_1)$.

2.7. Asymmetry between on-site energies: band gaps

2.7.1. Interlayer asymmetry. Interlayer asymmetry U , equation (25), describes a difference in the on-site energies of the orbitals on the two layers $\epsilon_{A1} = \epsilon_{B1} = -\epsilon_{A2} = -\epsilon_{B2} = -U/2$. Its influence on the bands $E = \pm \varepsilon_\alpha(p)$ is described by equation (31) with $v_3 = 0$:

$$\varepsilon_\alpha^2 = \frac{\gamma_1^2}{2} + \frac{U^2}{4} + v^2 p^2 + (-1)^\alpha \sqrt{\frac{\gamma_1^4}{4} + v^2 p^2 [\gamma_1^2 + U^2]}, \quad (43)$$

The low-energy bands, $\alpha = 1$, display a distinctive ‘Mexican hat’ shape with a band gap U_g between the conduction and

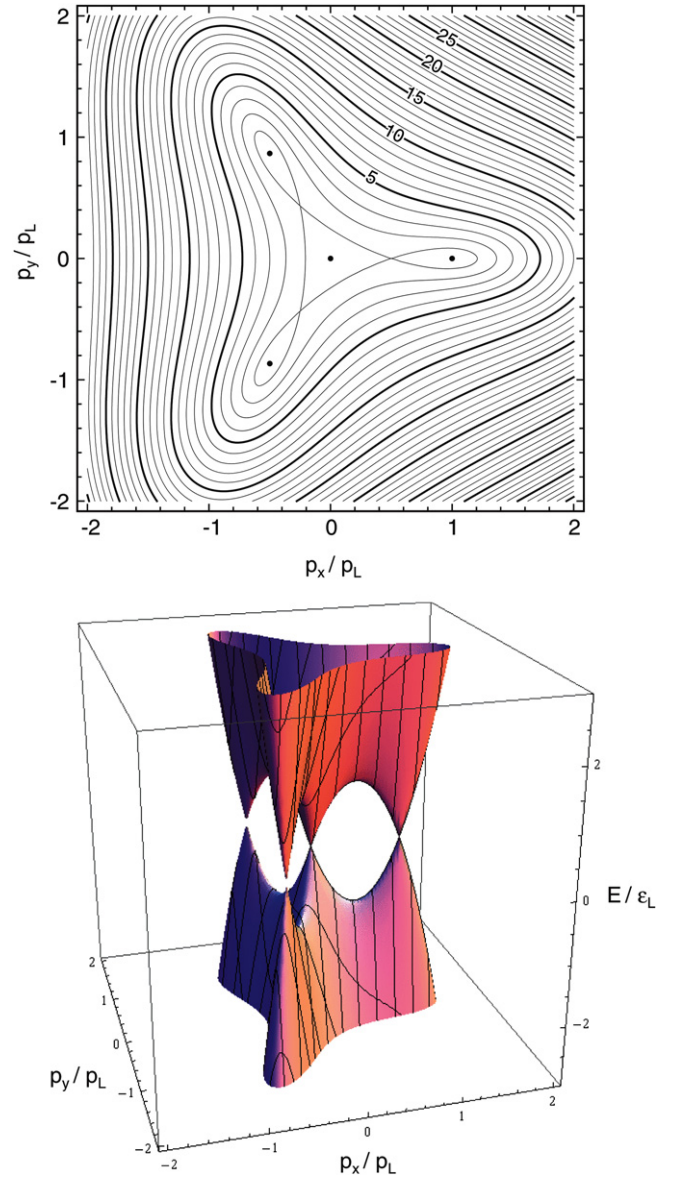


Figure 4. (a) Trigonal warping of the equi-energy lines in the vicinity of each K point, and the Lifshitz transition in bilayer graphene. The energy is in units of ε_L . (b) Corresponding three-dimensional plot of the low-energy dispersion.

valence bands which occurs at momentum p_g from the centre of the valley:

$$U_g = \frac{|U|\gamma_1}{\sqrt{\gamma_1^2 + U^2}}; \quad p_g = \frac{|U|}{2v} \sqrt{\frac{2\gamma_1^2 + U^2}{\gamma_1^2 + U^2}}. \quad (44)$$

For small values of the interlayer asymmetry U , the band gap is equal to the asymmetry $U_g = |U|$, but for large asymmetry values $|U| \gg \gamma_1$ the band gap saturates $U_g \rightarrow \gamma_1$. It is possible to induce interlayer asymmetry in bilayer graphene through doping [16] or the use of external gates [17, 19, 20]. This is described in detail in section 3.

2.7.2. Intralayer asymmetry between A and B sites. The energy difference δ_{AB} between A and B sites may be described

by the Hamiltonian (30) with $\epsilon_{A1} = -\epsilon_{B1} = \epsilon_{A2} = -\epsilon_{B2} = \delta_{AB}/2$ and $v_3 = v_4 = 0$, yielding bands $E = \pm \varepsilon_\alpha$:

$$\varepsilon_\alpha^2 = \frac{\delta_{AB}^2}{4} + \frac{\gamma_1^2}{4} \left[\sqrt{1 + 4v^2 p^2 / \gamma_1^2} + (-1)^\alpha \right]^2. \quad (45)$$

Thus, δ_{AB} creates a band gap, but there is no Mexican hat structure.

2.8. Next-nearest neighbour hopping

The terms described in Hamiltonians (16), (30) and (38) do not represent an exhaustive list of all possibilities. Additional coupling parameters may be taken into account. For example, next-nearest neighbour hopping within each layer [95–98] results in a term $(3 - |f(\mathbf{k})|^2)\gamma_n$ appearing on every diagonal element of the Hamiltonian (16), where γ_n is the coupling parameter between next-nearest A (or B) sites) on each layer. Ignoring the constant-in-momentum part $3\gamma_n$ produces an additional term in the two-component Hamiltonian (38)

$$\hat{h}_n = -\frac{\gamma_n v^2 p^2}{\gamma_0^2} \begin{pmatrix} 1 & 0 \\ 0 & 1 \end{pmatrix},$$

resulting in energies $E = \pm p^2/2m(1 \mp \gamma_n \gamma_1 / \gamma_0^2)$. Thus, next-nearest neighbour hopping represents another source of electron–hole asymmetry, after \hat{h}_4 , \hat{h}_Δ and S_b .

2.9. Spin–orbit coupling

For monolayer graphene, Kane and Mele [99] employed a symmetry analysis to show that there are two distinct types of spin–orbit coupling at the corners K_+ and K_- of the Brillouin zone. These two types of spin–orbit coupling also exist in bilayer graphene. In both monolayers and bilayers, the magnitude of spin–orbit coupling—although the subject of theoretical debate—is generally considered to be very small, with estimates roughly in the range 1–100 μeV [99–109].

At the corner of the Brillouin zone K_ξ in bilayer graphene, the contribution of spin–orbit coupling to the two-component low-energy Hamiltonian (38) may be written as

$$\hat{h}_{\text{SO}} = \lambda_{\text{SO}} \xi \sigma_z S_z, \quad (46)$$

$$\hat{h}_R = \lambda_R (\xi \sigma_x S_y + \sigma_y S_x), \quad (47)$$

where σ_i , $i = x, y, z$ are Pauli spin matrices in the $A1/B2$ sublattice space, and S_j , $j = x, y, z$ are Pauli spin matrices in the spin space. The first term \hat{h}_{SO} is intrinsic to graphene, i.e. it is a full invariant of the system. Both intra- and interlayer contributions to \hat{h}_{SO} have been discussed [105–107, 109] with the dominant contribution to its magnitude λ_{SO} attributed to skew interlayer coupling between π and σ orbitals [106, 107] or to the presence of unoccupied d orbitals within each graphene layer [109]. Taken with the quadratic term \hat{h}_0 in the Hamiltonian (38), \hat{h}_{SO} produces a gap of magnitude $2\lambda_{\text{SO}}$ in the spectrum of bilayer graphene, but the two low-energy bands remain spin and valley degenerate (as in a monolayer): $E = \pm \sqrt{\lambda_{\text{SO}}^2 + v^4 p^4 / \gamma_1^2}$. However, there

are gapless edge excitations and, like monolayer graphene [99], bilayer graphene in the presence of intrinsic spin–orbit coupling is a topological insulator with a finite spin Hall conductivity [110, 111].

The second type of spin–orbit coupling is the Bychkov–Rashba term \hat{h}_R , equation (47), which is permitted only if mirror reflection symmetry with respect to the graphene plane is broken, by the presence of an electric field or a substrate, say [99–101, 105, 110–116]. Taken with the quadratic term \hat{h}_0 in the Hamiltonian (38), \hat{h}_R does not produce a gap, but, as in the monolayer, spin-splitting of magnitude $2\lambda_R$ between the bands. That is, there are four valley-degenerate bands at low energies,

$$E^2 = \lambda_R^2 \left(\sqrt{1 + \frac{v^4 p^4}{\lambda_R^2 \gamma_1^2}} \pm 1 \right)^2. \quad (48)$$

Generally speaking, there is a rich interplay between tuneable interlayer asymmetry U and the influence of the intrinsic and the Bychkov–Rashba spin–orbit coupling in bilayer graphene [105, 110, 111, 115, 116]. For example, the presence of interlayer asymmetry U breaks inversion symmetry and allows for spin-split levels in the presence of intrinsic spin–orbit coupling only ($\lambda_R = 0$) [105], while the combination of finite U and very large Rashba coupling has been predicted to lead to a topological insulator state even with $\lambda_{\text{SO}} = 0$ [115].

2.10. The integer quantum Hall effect

When a two-dimensional electron gas is placed in a perpendicular magnetic field, electrons follow cyclotron orbits and their energies are quantized as Landau levels [117]. At a high enough magnetic field strength, the discrete nature of the Landau level spectrum is manifest as the integer quantum Hall effect [118–120], whereby the Hall conductivity assumes values that are integer multiples of the quantum of conductivity e^2/h .

The Landau level spectrum of monolayer graphene was calculated by McClure [121] nearly 60 years ago, and there have been a number of related theoretical studies [5, 6, 98, 122–124] considering the consequences of chirality in graphene. The experimental observation of the integer quantum Hall effect in monolayer graphene [2, 3] found an unusual sequencing of the quantized plateaus of Hall conductivity, confirming the chiral nature of the electrons and prompting an explosion of interest in the field [7]. In bilayer graphene, the observation of the integer quantum Hall effect [8] and the calculated Landau level spectrum [9] uncovered additional features related to the chiral nature of the electrons.

2.10.1. The Landau level spectrum of bilayer graphene. We consider the Landau level spectrum of the two-component chiral Hamiltonian \hat{h}_0 , equation (38). The magnetic field is accounted for by the operator $\mathbf{p} = (p_x, p_y) \equiv -i\hbar\nabla + e\mathbf{A}$ where \mathbf{A} is the vector potential and the charge of the electron is $-e$. For a magnetic field perpendicular to the bilayer, $\mathbf{B} = (0, 0, -B)$ where $B = |\mathbf{B}|$, the vector potential may be written in the Landau gauge $\mathbf{A} = (0, -Bx, 0)$, which

preserves translational invariance in the y direction. Then, $\pi = -i\hbar\xi\partial_x + \hbar\partial_y - ieBx$ and $\pi^\dagger = -i\hbar\xi\partial_x - \hbar\partial_y + ieBx$, and eigenstates are comprised of functions that are harmonic oscillator states in the x direction and plane waves in the y direction [119, 120],

$$\phi_\ell(x, y) = A_\ell \mathcal{H}_\ell\left(\frac{x}{\lambda_B} - \frac{p_y \lambda_B}{\hbar}\right) \times \exp\left[-\frac{1}{2}\left(\frac{x}{\lambda_B} - \frac{p_y \lambda_B}{\hbar}\right)^2 + i\frac{p_y y}{\hbar}\right], \quad (49)$$

where the magnetic length is $\lambda_B = \sqrt{\hbar/eB}$, \mathcal{H}_ℓ are Hermite polynomials of order ℓ for integer $\ell \geq 0$, and $A_\ell = 1/\sqrt{2^\ell \ell! \sqrt{\pi}}$ is a normalization constant.

The operators π and π^\dagger appearing in the Hamiltonian (38) act as raising and lowering operators for the harmonic oscillator states (49). At the first valley, K_+ ,

$$K_+ : \quad \pi \phi_\ell = -\frac{\sqrt{2i}\hbar}{\lambda_B} \sqrt{\ell} \phi_{\ell-1}, \quad (50)$$

$$K_+ : \quad \pi^\dagger \phi_\ell = \frac{\sqrt{2i}\hbar}{\lambda_B} \sqrt{\ell+1} \phi_{\ell+1}, \quad (51)$$

and $\pi \phi_0 = 0$. Then, it is possible to show that the Landau level spectrum of the Hamiltonian (38) consists of a series of electron and hole levels with energies and wave functions [9] given by

$$E_{\ell,\pm} = \pm \hbar \omega_c \sqrt{\ell(\ell-1)}, \quad \ell \geq 2, \quad (52)$$

$$K_+ : \quad \psi_{\ell,\pm} = \frac{1}{\sqrt{2}} \begin{pmatrix} \phi_\ell \\ \pm \phi_{\ell-2} \end{pmatrix}, \quad \ell \geq 2, \quad (53)$$

where $\omega_c = eB/m$ and \pm refer to the electron and hole states, respectively. For high values of the index, $\ell \gg 1$, the levels are approximately equidistant with spacing $\hbar \omega_c$ proportional to the magnetic field strength B . However, this spectrum, equation (52), is only valid for sufficiently small level index and magnetic field $\ell \hbar \omega_c \ll \gamma_1$ because the effective Hamiltonian (38) is only applicable at low energies.

In addition to the field-dependent levels, there are two levels fixed at zero energy $E_1 = E_0 = 0$ with eigenfunctions:

$$K_+ : \quad \psi_1 = \begin{pmatrix} \phi_1 \\ 0 \end{pmatrix}, \quad \psi_0 = \begin{pmatrix} \phi_0 \\ 0 \end{pmatrix}, \quad (54)$$

They may be viewed as arising from the square of the lowering operator in the Hamiltonian (38) which acts on both the oscillator ground state and the first excited state to give zero energy $\pi^2 \phi_0 = \pi^2 \phi_1 = 0$. The eigenfunctions ψ_0 and ψ_1 have a finite amplitude on the $A1$ sublattice, on the bottom layer, but zero amplitude on the $B2$ sublattice.

At the second valley, K_- , the roles of operators π and π^\dagger are reversed:

$$K_- : \quad \pi \phi_\ell = -\frac{\sqrt{2i}\hbar}{\lambda_B} \sqrt{\ell+1} \phi_{\ell+1}, \quad (55)$$

$$K_- : \quad \pi^\dagger \phi_\ell = \frac{\sqrt{2i}\hbar}{\lambda_B} \sqrt{\ell} \phi_{\ell-1}, \quad (56)$$

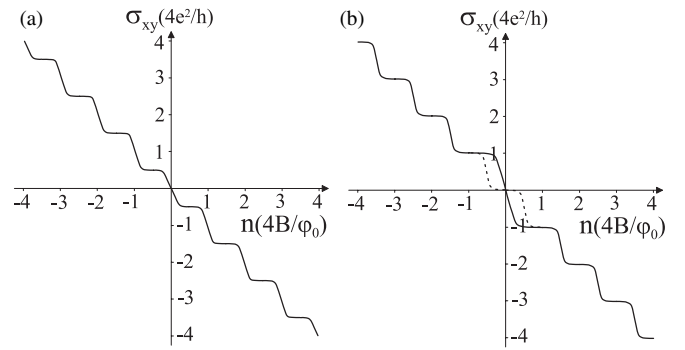


Figure 5. Schematic of the dependence of the Hall conductivity σ_{xy} on carrier density n for (a) monolayer graphene and (b) bilayer graphene, where $\varphi_0 = h/e$ is the flux quantum and B is the magnetic field strength. The dashed line in (b) shows the behaviour for a conventional semiconductor or bilayer graphene in the presence of large interlayer asymmetry U (section 2.10.3) with fourfold level degeneracy due to spin and valley degrees of freedom.

and $\pi^\dagger \phi_0 = 0$. The Landau level spectrum at K_- is degenerate with that at K_+ , i.e. $E_{\ell,\pm} = \pm \hbar \omega_c \sqrt{\ell(\ell-1)}$ for $\ell \geq 2$ and $E_1 = E_0 = 0$, but the roles of the $A1$ and $B2$ sublattices are reversed:

$$K_- : \quad \psi_{\ell,\pm} = \frac{1}{\sqrt{2}} \begin{pmatrix} \phi_{\ell-2} \\ \pm \phi_\ell \end{pmatrix}, \quad \ell \geq 2, \quad (57)$$

$$K_- : \quad \psi_1 = \begin{pmatrix} 0 \\ \phi_1 \end{pmatrix}, \quad \psi_0 = \begin{pmatrix} 0 \\ \phi_0 \end{pmatrix}, \quad (58)$$

The valley structure and electronic spin each contribute a twofold degeneracy to the Landau level spectrum. Thus, each level in bilayer level graphene is fourfold degenerate, except for the zero energy levels which have eightfold degeneracy due to valley, spin and the orbital degeneracy of ψ_0, ψ_1 .

2.10.2. Three types of integer quantum Hall effect. The form of the Landau level spectrum is manifest in a measurement of the integer quantum Hall effect. Here, we will compare the density dependence of the Hall conductivity $\sigma_{xy}(n)$ for bilayer graphene with that of a conventional semiconductor and of monolayer graphene.

The Landau level spectrum of a conventional two-dimensional semiconductor is $E_\ell = \hbar \omega_c (\ell + 1/2)$, $\ell \geq 0$, where $\omega_c = eB/m$ is the cyclotron frequency [119, 120]. As density is changed, there is a step in σ_{xy} whenever a Landau level is crossed, and the separation of steps on the density axis is equal to the maximum carrier density per Landau level, gB/φ_0 , where $\varphi_0 = h/e$ is the flux quantum and g is a degeneracy factor. Each plateau of the Hall conductivity σ_{xy} occurs at a quantized value of Nge^2/h where N is an integer labelling the plateau and g is an integer describing the level degeneracy; steps between adjacent plateaus have height ge^2/h .

The Landau level spectrum of monolayer graphene [98, 121–124] consists of an electron and a hole series of levels, $E_{\ell,\pm} = \pm \sqrt{2\ell} \hbar v / \lambda_B$ for $\ell \geq 1$, with an additional level at zero energy $E_0 = 0$. All of the levels are fourfold degenerate, due to spin and valley degrees of freedom. The corresponding Hall conductivity is shown schematically in figure 5(a). There

are steps of height $4e^2/h$ between each plateau, as expected by consideration of the conventional case, but the plateaus occur at half-integer values of $4e^2/h$ instead of integer ones, as observed experimentally [2, 3]. This is due to the existence of the fourfold-degenerate level $E_0 = 0$ at zero energy, which contributes to a step of height $4e^2/h$ at zero density.

For bilayer graphene, plateaus in the Hall conductivity $\sigma_{xy}(n)$, figure 5(b), occur at integer multiples of $4e^2/h$. This is similar to a conventional semiconductor with level degeneracy $g = 4$ arising from the spin and valley degrees of freedom. Deviation from the conventional case occurs at low densities. In the bilayer there is a step in σ_{xy} of height $8e^2/h$ across zero density, accompanied by a plateau separation of $8B/\varphi_0$ in density [8, 9], arising from the eightfold degeneracy of the zero-energy Landau levels. This is shown as the solid line in figure 5(b), whereas, for a conventional semiconductor, there is no step across zero density (the dashed line).

Thus, the chirality of charge carriers in monolayer and bilayer graphene give rise to four- and eightfold degenerate Landau levels at zero energy and to steps of height of four and eight times the conductance quantum e^2/h in the Hall conductivity at zero density [2, 3, 8]. Here, we have assumed that the degeneracy of the Landau levels is preserved, i.e. any splitting of the levels is negligible as compared with temperature and level broadening in an experiment. The role of electronic interactions in bilayer graphene is described in section 8, while we discuss the influence of interlayer asymmetry on the Landau level spectrum and integer quantum Hall effect in the next section.

2.10.3. The role of interlayer asymmetry. The Landau level states, equations (53) and (57), have different amplitudes on the lower ($A1$ sublattice) and upper ($B2$ sublattice) layers, with the role of the sublattice sites swapped at the two valleys. Thus, interlayer asymmetry U as described by the effective Hamiltonian \hat{h}_U , equation (38), leads to a weak splitting of the valley degeneracy of the levels [9]:

$$E_{\ell,\pm} \approx \pm \hbar\omega_c \sqrt{\ell(\ell-1)} + \frac{\xi U \hbar\omega_c}{2\gamma_1}. \quad (59)$$

Such a splitting is prominent for the zero-energy states [9], equations (54) and (58), because they only have non-zero amplitude on one of the layers, depending on the valley:

$$E_0 = -\frac{1}{2}\xi U, \quad (60)$$

$$E_1 = -\frac{1}{2}\xi U + \frac{\xi U \hbar\omega_c}{\gamma_1}. \quad (61)$$

When the asymmetry is large enough, then the splitting U of the zero energy levels from each valley results in a sequence of quantum Hall plateaus at all integer values of $4e^2/h$ including a plateau at zero density [17], as observed experimentally [20]. This behaviour is shown schematically as the dashed line in figure 5(b). The Landau level spectrum in the presence of large interlayer asymmetry U has been calculated [125–128], including an analysis of level crossings [128] and a self-consistent calculation of the spectrum in the presence of an external gate [126, 127], generalizing the zero-field procedure outlined in the next section.

3. Tuneable band gap

3.1. Experiments

A tuneable band gap in bilayer graphene was first observed with angle-resolved photoemission of epitaxial bilayer graphene on silicon carbide [16], and the ability to control the gap was demonstrated by doping with potassium. Since then, the majority of experiments probing the band gap have used single or dual gate devices based on exfoliated bilayer graphene flakes [19, 20]. The band gap has now been observed in a number of different experiments including photoemission [16], magnetotransport [20], infrared spectroscopy [55, 78–80, 129, 130], electronic compressibility [131, 132], scanning tunnelling spectroscopy [133], and transport [19, 31, 134–139].

The gap observed in optics [16, 55, 78–80, 129, 130] is up to 250 meV [129, 130], the value expected theoretically (as the gap should saturate at the value of the interlayer coupling γ_1). Transport measurements show insulating behaviour [19, 31, 134–139], but, generally, not the huge suppression of conductivity expected for a gap of this magnitude, and this has been attributed to edge states [140], the presence of disorder [141–143] or disorder and chiral charge carriers [144]. Broadly speaking, transport seems to occur through different mechanisms in different temperature regimes with thermal activation [31, 134–136, 138, 139] at high temperatures (above, roughly, 2–50 K) and variable-range [19, 135–137, 139] or nearest-neighbour hopping [135, 138] at low temperatures.

3.2. Hartree model of screening

External gates are generally used to control the density of electrons n on a graphene device [1], but, in bilayer graphene, external gates will also place the separate layers of the bilayer at different potential energies resulting in interlayer asymmetry $U = \epsilon_2 - \epsilon_1$ (where $\epsilon_1 = \epsilon_{A1} = \epsilon_{B1} = -U/2$ and $\epsilon_2 = \epsilon_{A2} = \epsilon_{B2} = U/2$). Thus, changing the applied gate voltage(s) will tend to tune both the density n and the interlayer asymmetry U , and, ultimately, the band gap U_g . The dependence of the band gap on the density $U_g(n)$ relies on screening by electrons on the bilayer. In the following, we describe a simple model [17, 18, 20, 55, 69, 71, 145, 146] that has been developed to take into account screening using the tight-binding model and Hartree theory.

3.2.1. Electrostatics: asymmetry parameter, layer densities and external gates. We use the SI system of units, and the electronic charge is $-e$ where $e > 0$. The bilayer graphene device is modelled as two parallel conducting plates that are very narrow in the x -direction, continuous and infinite in the y – z plane, positioned at $x = -c_0/2$ and $+c_0/2$, figure 6. Here, c_0 is the interlayer spacing and we denote the dielectric constant of the interlayer space as ϵ_r (it does not include the screening by π -band electrons that we are explicitly modelling). Layer number densities are n_1 and n_2 , with corresponding charge densities $\sigma_1 = -en_1$ and $\sigma_2 = -en_2$.

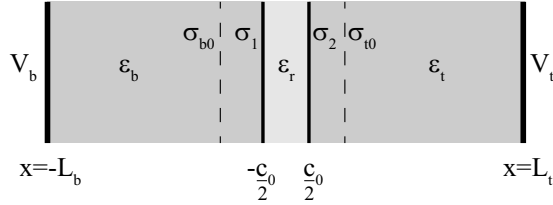


Figure 6. Schematic of bilayer graphene in the presence of external gates located at $x = -L_b$ and $x = +L_t$, with potentials V_b and V_t , which are separated from the bilayer by media of dielectric constants ε_b and ε_t , respectively. The bilayer is modelled as two parallel conducting plates positioned at $x = -c_0/2$ and $x = c_0/2$, separated by a region of dielectric constant ε_r . The layers have charge densities $\sigma_1 = -en_1$ and $\sigma_2 = -en_2$ corresponding to layer number densities n_1 and n_2 . Charge densities σ_{b0} and σ_{t0} (dashed lines) arise from the presence of additional charged impurities.

We take into account the presence of a back gate and a top gate, infinite in the y - z plane, located at $x = -L_b$ and $x = +L_t$, with potentials V_b and V_t , which are separated from the bilayer by media of dielectric constants ε_b and ε_t , respectively. It is possible to describe the presence of additional charge near the bilayer—due to impurities, say—by introducing density n_{b0} on the back-gate side and n_{t0} on the top-gate side. They correspond to charge densities $\sigma_{b0} = en_{b0}$ and $\sigma_{t0} = en_{t0}$, assuming that n_{b0} and n_{t0} are positive for positive charge.

Using Gauss's law, it is possible to relate the external gate potentials and impurity concentrations to the layer densities and the interlayer asymmetry [17, 60, 145, 147]:

$$n = n_1 + n_2 = \frac{\varepsilon_0 \varepsilon_b V_b}{e L_b} + \frac{\varepsilon_0 \varepsilon_t V_t}{e L_t} + n_{b0} + n_{t0}, \quad (62)$$

$$U = -\frac{\varepsilon_t}{\varepsilon_r} \frac{c_0}{L_t} e V_t + \frac{e^2 c_0}{\varepsilon_0 \varepsilon_r} (n_2 - n_{t0}), \quad (63)$$

where the field within the bilayer interlayer space is approximately equal to $U/(ec_0)$. Equation (62) expresses the total electron density $n = n_1 + n_2$ in terms of the external potentials, generalizing the relation for monolayer graphene [1]. Note that the background densities n_{b0} and n_{t0} shift the effective values of the gate potentials V_b and V_t . The second equation, for U , may be rewritten as

$$U = U_{\text{ext}} + \Lambda \gamma_1 \frac{(n_2 - n_1)}{n_{\perp}}, \quad (64)$$

$$U_{\text{ext}} = \frac{ec_0}{2\varepsilon_r} \left(\frac{\varepsilon_b}{L_b} V_b - \frac{\varepsilon_t}{L_t} V_t \right) + \Lambda \gamma_1 \frac{(n_{b0} - n_{t0})}{n_{\perp}}, \quad (65)$$

where the characteristic density scale n_{\perp} and the dimensionless screening parameter Λ are

$$n_{\perp} = \frac{\gamma_1^2}{\pi \hbar^2 v^2}, \quad \Lambda = \frac{c_0 e^2 \gamma_1}{2\pi \hbar^2 v^2 \varepsilon_0 \varepsilon_r} \equiv \frac{c_0 e^2 n_{\perp}}{2\gamma_1 \varepsilon_0 \varepsilon_r}. \quad (66)$$

Equation (64) relates the asymmetry parameter U to a sum of its value, U_{ext} , if screening were negligible plus a term accounting for screening. Parameter values $\gamma_1 = 0.39$ eV and $v = 1.0 \times 10^6$ ms⁻¹ give $n_{\perp} = 1.1 \times 10^{13}$ cm⁻². With interlayer spacing $c_0 = 3.35$ Å and an estimate for the dielectric constant of $\varepsilon_r \approx 1$, then $\Lambda \sim 1$, showing that screening is relevant.

3.2.2. Calculation of individual layer densities. Through electrostatics, the asymmetry parameter U is related to layer densities n_1 and n_2 , equation (64). The densities n_1 and n_2 also depend on U because of the band structure of bilayer graphene. Analytical calculations are possible [17, 18, 145] if only the dominant interlayer coupling γ_1 is taken into account in the four-band Hamiltonian (30). Here we will use the two-band model (38) with an explicit ultraviolet cutoff [18] when integrating over the whole Brillouin zone. The simplified two-component Hamiltonian is

$$\hat{H}_2 \approx -\frac{v^2}{\gamma_1} \begin{pmatrix} 0 & (\pi^\dagger)^2 \\ \pi^2 & 0 \end{pmatrix} - \frac{U}{2} \begin{pmatrix} 1 & 0 \\ 0 & -1 \end{pmatrix}, \quad (67)$$

Solutions to the energy eigenvalue equation $\hat{H}_2 \psi = E \psi$ are given by

$$E = \pm \sqrt{\frac{U^2}{4} + \frac{v^4 p^4}{\gamma_1^2}}, \quad (68)$$

$$\psi = \sqrt{\frac{E - U/2}{2E}} \begin{pmatrix} 1 \\ -\frac{v^2 p^2}{\gamma_1 (E - U/2)} e^{2i\xi\varphi} \end{pmatrix} e^{ip \cdot r/\hbar}. \quad (69)$$

Layer densities are determined by integration over the circular Fermi surface

$$n_{1(2)} = \frac{2}{\pi \hbar^2} \int |\psi_{A1(B2)}(p)|^2 p \, dp, \quad (70)$$

where a factor of four takes account of spin and valley degeneracy.

For simplicity, we assume the Fermi energy lies within the conduction band. Using the solution (69), the contribution of the partially filled conduction band to the layer densities [17, 145, 148] is given by

$$\begin{aligned} n_{1(2)}^{\text{cb}} &= \frac{1}{\pi \hbar^2} \int p \, dp \left(\frac{E \mp U/2}{E} \right), \\ &= \frac{1}{\pi \hbar^2} \int_0^{p_F} p \, dp \mp \frac{U}{2\pi \hbar^2} \int_0^{p_F} \frac{p \, dp}{\sqrt{U^2/4 + v^4 p^4/\gamma_1^2}}, \\ &\approx \frac{n}{2} \mp \frac{n_{\perp} U}{4\gamma_1} \ln \left(\frac{2|n|\gamma_1}{n_{\perp}|U|} + \sqrt{1 + \left(\frac{2n\gamma_1}{n_{\perp}U} \right)^2} \right), \end{aligned} \quad (71)$$

where the minus (plus) sign is for the first (second) layer, p_F is the Fermi momentum, and the total density is $n = p_F^2/\pi \hbar^2$ measured with respect to the charge-neutrality point, i.e. we assume that the point of zero density is realized when the Fermi level lies at the crossing point of the conduction and valence bands.

In addition, we take into account the contribution of the filled valence band $n_{1(2)}^{\text{vb}}$ to the individual layer densities. Note that, as the asymmetry parameter U varies, the filled valence band does not contribute to any change in the total density n , but it does contribute to the difference $n_1 - n_2$. This may be obtained by integrating with respect to momentum as in equation (71), but introducing an ultraviolet cutoff $p_{\text{max}} = \gamma_1/v$ equivalent to $n_{\text{max}} = n_{\perp}$ [18]. Then, the contribution of

the filled valence band [17, 18, 69, 71, 145, 146] is given by

$$n_{1(2)}^{\text{vb}} \approx \pm \frac{U}{2\pi\hbar^2} \int_0^{p_{\text{max}}} \frac{p \, dp}{\sqrt{U^2/4 + v^4 p^4/\gamma_1^2}},$$

$$\approx \pm \frac{n_{\perp} U}{4\gamma_1} \ln \left(\frac{4\gamma_1}{|U|} \right). \quad (72)$$

Combining the contributions of equations (71) and (72), the individual layer density, $n_{1(2)} = n_{1(2)}^{\text{cb}} + n_{1(2)}^{\text{vb}}$, is given [17, 145] by

$$n_{1(2)} \approx \frac{n}{2} \mp \frac{n_{\perp} U}{4\gamma_1} \ln \left(\frac{|n|}{2n_{\perp}} + \frac{1}{2} \sqrt{\left(\frac{n}{n_{\perp}} \right)^2 + \left(\frac{U}{2\gamma_1} \right)^2} \right). \quad (73)$$

Note that some calculations [148] include only the contribution (71) of the partially filled conduction band, others [18] include only the filled valence band (72).

3.2.3. Self-consistent screening. Substituting the layer density (73) into the expression (64) describing screening gives an expression [17, 60, 145] for the density dependence of the asymmetry parameter U :

$$\frac{U(n)}{U_{\text{ext}}} \approx \left[1 - \frac{\Lambda}{2} \ln \left(\frac{|n|}{2n_{\perp}} + \frac{1}{2} \sqrt{\left(\frac{n}{n_{\perp}} \right)^2 + \left(\frac{U}{2\gamma_1} \right)^2} \right) \right]^{-1}, \quad (74)$$

where U_{ext} is the asymmetry in the absence of screening (65). The extent of screening is described by the logarithmic term with argument depending on n and U , and a prefactor proportional to the screening parameter $\Lambda \sim 1$ (as discussed earlier). A common experimental setup, especially for exfoliated graphene on a silicon substrate [1–3, 8], includes a single back gate. Figure 7 shows the density dependence of the band gap $U_g(n)$ plotted as the back-gate voltage V_b is varied for a fixed top-gate voltage V_t . In this case, the influence of the top-gate voltage V_t may be absorbed into an effective offset-density $n_0 = 2[\varepsilon_0 \varepsilon_t V_t / (eL_t) + n_{t0}]$ [17] giving $U_{\text{ext}} = \Lambda \gamma_1 (n - n_0) / n_{\perp}$ in equation (74). Figure 8 shows the dependence of the difference in layer densities $n_1 - n_2$ for the case $n_0 = 0$ including both the contribution of the partially filled bands as measured with respect to the charge-neutrality point (71) (dashed line) and the contribution of the full valence band (72) (dotted line). The sum of both terms (solid line) shows that $n_1 - n_2$ is positive (negative) for positive (negative) total density n . Recalling that layer 1 is closest to the back gate, this shows that the bilayer is polarized along the electric field, as expected [145].

A single back gate in the absence of additional charged dopants may be described by $V_t = n_{b0} = n_{t0} = 0$, resulting in simplified expressions $n = \varepsilon_0 \varepsilon_b V_b / (eL_b)$ (as in monolayer graphene [1]) and $U_{\text{ext}} = \Lambda \gamma_1 n / n_{\perp}$. Using $|U| \ll \gamma_1$, equation (74) simplifies [17, 60, 69, 71] as

$$U(n) \approx \frac{\Lambda \gamma_1 n}{n_{\perp}} \left[1 - \frac{\Lambda}{2} \ln \left(\frac{|n|}{n_{\perp}} \right) \right]^{-1}, \quad (75)$$

At high density $|n| \sim n_{\perp}$, the logarithmic term is negligible and $U(n) \approx \Lambda \gamma_1 n / n_{\perp}$ is approximately linear in density. Note

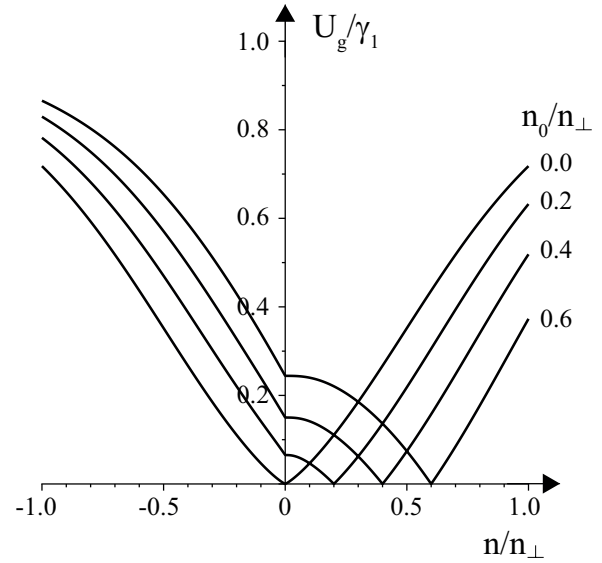


Figure 7. Density dependence of the band gap $U_g(n)$ in bilayer graphene as the back-gate voltage V_b is varied for a fixed top-gate voltage V_t [17]. The effective offset-density is $n_0 = 2[\varepsilon_0 \varepsilon_t V_t / (eL_t) + n_{t0}]$. Plots were made for screening parameter $\Lambda = 1$, using $U_g = |U| \gamma_1 / \sqrt{U^2 + \gamma_1^2}$ and numerical solution of equation (74).

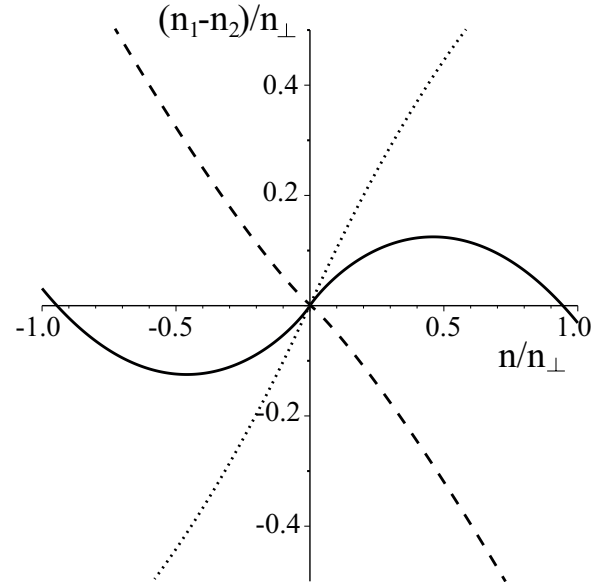


Figure 8. Density dependence of the difference in layer densities $n_1 - n_2$ in bilayer graphene as the back-gate voltage V_b is varied for a fixed top-gate voltage V_t [17]. Plots were made for screening parameter $\Lambda = 1$ and the effective offset-density is $n_0 = 2[\varepsilon_0 \varepsilon_t V_t / (eL_t) + n_{t0}] = 0$, corresponding to the data labelled $n_0 = 0$ in figure 7, obtained by numerical solution of equation (74). The dashed line shows the contribution of the partially filled bands as measured with respect to the charge-neutrality point (71) [148], the dotted line shows the contribution of the full valence band (72) [18], the solid line is their sum (73) [17, 145].

that the band gap $U_g = |U| \gamma_1 / \sqrt{U^2 + \gamma_1^2}$ tends to saturate $U_g \rightarrow \gamma_1$, even if $|U| \gg \gamma_1$. At low densities, $|n| \ll n_{\perp}$, the logarithmic term describing screening dominates and $U_g \approx |U| \approx 2\gamma_1 (|n| / n_{\perp}) / \ln(n_{\perp} / |n|)$, independent of the screening parameter Λ .

Expressions (74) and (75) for $U(n)$ take into account screening due to low-energy electrons in p_z orbitals using a simplified Hamiltonian (67) while neglecting other orbitals and the effects of disorder [55, 145, 149–155], crystalline inhomogeneity [18] and electron–electron exchange and correlation. Nevertheless, there is generally good qualitative agreement of the dependence of $U(n)$ on density n predicted by equations (74) and (75) with density-functional theory calculations [18, 73] and experiments including photoemission [16, 20] and infrared spectroscopy [55, 78–80, 129, 130]. Note that the Hartree screening model has been generalized to describe graphene trilayers and multilayers [147, 156–158].

4. Transport properties

4.1. Introduction

Bilayer graphene exhibits peculiar transport properties due to its unusual band structure, described in section 2, where the conduction and valence bands touch with quadratic dispersion. Transport characteristics and the nature of conductivity near the Dirac point were probed experimentally [2, 3, 8, 19, 20, 159–162] and investigated theoretically [163–175]. Neglecting trigonal warping, the minimal conductivity is predicted to be $8e^2/(\pi h)$ [163, 167, 168], twice the value in monolayer graphene, while, in the presence of trigonal warping, it is larger, $24e^2/(\pi h)$ [163, 169], because of multiple Fermi surface pockets at low energies, section 2.5.

For a detailed review of the electronic transport properties of graphene monolayer and bilayers, see [176, 177]. The characteristics of bilayer graphene in the presence of short-ranged defects and long-ranged charged-impurities have been calculated [54, 163, 164, 166, 171–175] and it is predicted that the conductivity has an approximately linear dependence on density at typical experimental densities [172]. At interfaces and potential barriers, conservation of the pseudospin degree of freedom may influence electronic transmission [178, 179], as in monolayer graphene [178, 180], including transmission at monolayer–bilayer interfaces [181–184], through multiple electrostatic barriers [185], or magnetic barriers [186, 187]. Inducing interlayer asymmetry and a band gap using an external gate [9, 17], described in section 3, may be used to tune transport properties [181, 188]. Interlayer asymmetry may also be viewed as creating an out-of-plane component of pseudospin and interfaces between regions of opposite polarity have attracted theoretical attention due to the existence of one-dimensional valley-polarized modes along the interface [189–192], a pseudospinronic analogy of spin-valve devices for transport perpendicular to the interface [193, 194], electronic confinement [195], and valley-dependent transmission [196].

In the following we describe two different models of the conductivity of bilayer graphene at low energies. The first is for ballistic transport in a clean device of finite length that is connected to semi-infinite leads, described using wave matching to calculate the transmission probability and, then, the conductance. The second model describes the conductivity of a disordered, infinite system using the Kubo formula and

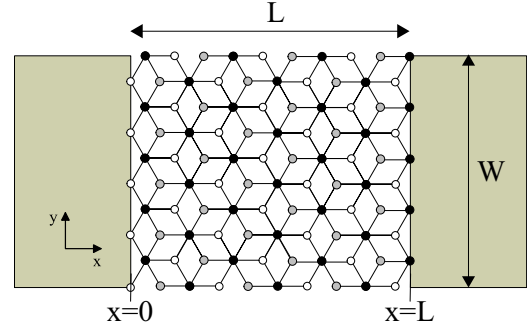


Figure 9. Two-probe bilayer graphene device with armchair edges, width W and length L . The rectangular shaded regions represent the ends of semi-infinite leads.

the self-consistent Born approximation to describe scattering from the disordered potential. Although the two models are quite different, both predict the minimal conductivity to be $8e^2/(\pi h)$ [163, 167, 168]. Finally, in section 4.3.2, we describe localization effects.

4.2. Ballistic transport in a finite system

Ballistic transport in a finite, mesoscopic bilayer graphene nanostructure has been modelled in a number of papers [165, 167–169, 178, 193, 194, 196]. Here, we follow a wave-matching approach of Snyman and Beenakker [168]. For bilayer, as compared with monolayer, there is a new length scale $\ell_1 = \hbar v/\gamma_1$ characteristic of the interlayer coupling. Here, $v = \sqrt{3}a\gamma_0/2\hbar$ is the band velocity of monolayer graphene, so $\ell_1 = (\sqrt{3}/2)(\gamma_0/\gamma_1)a \approx 18 \text{ \AA}$ is several times longer [168] than the lattice constant $a = 2.46 \text{ \AA}$ [53]. For most situations, the sample size $L \gg \ell_1$, and the device generally behaves as a (coupled) bilayer rather than two separate monolayers [168].

We consider a two-probe geometry with armchair edges as shown in figure 9. There is a central mesoscopic bilayer region, width W and length L , connected to a left and right lead. This orientation is rotated by 90° as compared with that described in section 2 so the corners of the Brillouin zone are located at wavevectors $\mathbf{K}_\xi = \xi(0, 4\pi/3a)$. In terms of wavevector measured from the centre of the valley, i.e. $k_y \rightarrow k_y + \xi 4\pi/3a$, then the Hamiltonian (30) in basis $A1, B1, A2, B2$ may be written as

$$H_b = \begin{pmatrix} U & v\pi^\dagger & 0 & 0 \\ v\pi & U & \gamma_1 & 0 \\ 0 & \gamma_1 & U & v\pi^\dagger \\ 0 & 0 & v\pi & U \end{pmatrix}, \quad (76)$$

where $\pi = -i\hbar(k_x + i\xi k_y)$, $\pi^\dagger = i\hbar(k_x - i\xi k_y)$, and U is the on-site energy which describes the doping of the bilayer. For simplicity, we include only the main interlayer coupling term γ_1 of the orbitals on the dimer $B1$ and $A2$ sites. It is assumed that the transverse wavevector k_y is real and it is conserved at the interfaces between the bilayer and the leads. The Hamiltonian (76) shows there are two values of the longitudinal wavevector k_x for given U , k_y and energy ε ,

which we denote as k_+ and k_- :

$$\hbar v k_{\pm} = \sqrt{(\varepsilon - U)^2 \pm \gamma_1(\varepsilon - U) - \hbar^2 v^2 k_y^2}. \quad (77)$$

Left- Φ_{\pm}^L and right- Φ_{\pm}^R moving wave functions may be written as

$$\Phi_{\pm}^L = N_{\pm} \begin{pmatrix} \mp i \hbar v (-k_{\pm} - i \xi k_y) \\ \mp (\varepsilon - U) \\ (\varepsilon - U) \\ -i \hbar v (-k_{\pm} + i \xi k_y) \end{pmatrix} e^{-i k_{\pm} x + i k_y y}, \quad (78)$$

$$\Phi_{\pm}^R = N_{\pm} \begin{pmatrix} \mp i \hbar v (k_{\pm} - i \xi k_y) \\ \mp (\varepsilon - U) \\ (\varepsilon - U) \\ -i \hbar v (k_{\pm} + i \xi k_y) \end{pmatrix} e^{i k_{\pm} x + i k_y y}, \quad (79)$$

where normalization $N_{\pm} = [4W(\varepsilon - U)k_{\pm}]^{-1/2}$ for unit current.

The aim is to describe a mesoscopic bilayer region of finite length L connected to macroscopic leads. In order to mimic macroscopic, metallic contacts, there should be many propagating modes in the leads that overlap with the modes in the central bilayer region. If this is the case, then the value of minimal conductance should not depend on the particular model used for the leads, e.g. square lattice or graphene lattice, as demonstrated for monolayer graphene [197]. Note, this will yield quite different results from a model with a bilayer lead at the same level of doping as the central region; then, the system is effectively an infinite system, not a finite, mesoscopic conductor.

Snyman and Beenakker [168] modelled the leads as heavily doped bilayer graphene, generalizing an approach developed for monolayer graphene [198]. In this way, there are many conducting modes present in the leads and it is possible to simply use matching of the bilayer wave functions at the interface between the central region and the leads. In particular, the leads are modelled as bilayer graphene with on-site energy $U = -U_{\infty}$, where $U_{\infty} > 0$ and $U_{\infty} \gg \{|\varepsilon|, \gamma_1\}$. Then, in the leads, $k_+ \approx k_- \approx U_{\infty}/(\hbar v)$ and wave functions $\psi_{\text{left},\pm}$, $\psi_{\text{right},\pm}$, in the left ($x < 0$) and right ($x > L$) leads may be written as

$$\psi_{\text{left},\pm} = \left[\begin{pmatrix} \mp i \\ \mp 1 \\ 1 \\ -i \end{pmatrix} e^{i U_{\infty} x / \hbar v} + r_{\pm}^{\pm} \begin{pmatrix} i \\ -1 \\ 1 \\ i \end{pmatrix} e^{-i U_{\infty} x / \hbar v} + r_{\pm}^{\pm} \begin{pmatrix} -i \\ 1 \\ 1 \\ i \end{pmatrix} e^{-i U_{\infty} x / \hbar v} \right] e^{i k_y y}, \quad (80)$$

$$\psi_{\text{right},\pm} = \left[t_{\pm}^{\pm} \begin{pmatrix} -i \\ -1 \\ 1 \\ -i \end{pmatrix} + t_{\pm}^{\pm} \begin{pmatrix} i \\ 1 \\ 1 \\ -i \end{pmatrix} \right] e^{i U_{\infty} (x-L) / \hbar v + i k_y y}. \quad (81)$$

Here, a right-moving wave with unit flux corresponding to a state with wavevector $k_{\pm} \approx U_{\infty}/(\hbar v)$ is injected from the left lead (the first term in equation (80)). Subsequently, there are two left-moving waves that have been reflected

with amplitudes r_{\pm}^{\pm} and r_{\pm}^{\mp} , and two right-moving waves are transmitted to the right, with amplitudes t_{\pm}^{\pm} and t_{\pm}^{\mp} .

At the charge-neutrality point $\varepsilon = U = 0$ in the central bilayer region, the wave functions are evanescent with imaginary longitudinal wavevector, equation (77). Two states with $k_x = -i \xi k_y$ have finite amplitude only on the $A1, A2$ sites and two with $k_x = i \xi k_y$ have finite amplitude only on the $B1, B2$ sites:

$$\psi_{\text{centre},\pm} = \left[c_1^{\pm} \begin{pmatrix} 1 \\ 0 \\ 0 \\ 0 \end{pmatrix} e^{\xi k_y y} + c_2^{\pm} \begin{pmatrix} \gamma_1 x / \hbar v \\ 0 \\ 1 \\ 0 \end{pmatrix} e^{\xi k_y y} \right] \quad (82)$$

$$+ c_3^{\pm} \begin{pmatrix} 0 \\ 1 \\ 0 \\ -\gamma_1 x / \hbar v \end{pmatrix} e^{-\xi k_y y} + c_4^{\pm} \begin{pmatrix} 0 \\ 0 \\ 0 \\ 1 \end{pmatrix} e^{-\xi k_y y} \Big] e^{i k_y y}. \quad (83)$$

For each incoming mode \pm from the left lead (the first term in equation (80)), there are eight unknown amplitudes $c_1^{\pm}, c_2^{\pm}, c_3^{\pm}, c_4^{\pm}, r_{\pm}^{\pm}, r_{\pm}^{\mp}, t_{\pm}^{\pm}, t_{\pm}^{\mp}$. Continuity of the wave functions at the interfaces $x = 0$ and $x = L$ between the central region and the leads provides eight simultaneous equations:

$$\mp i + i r_{\pm}^{\pm} - i r_{\pm}^{\mp} = c_1^{\pm}, \quad (84)$$

$$\mp 1 - r_{\pm}^{\pm} + r_{\pm}^{\mp} = c_3^{\pm}, \quad (85)$$

$$1 + r_{\pm}^{\pm} + r_{\pm}^{\mp} = c_2^{\pm}, \quad (86)$$

$$-i + i r_{\pm}^{\pm} + i r_{\pm}^{\mp} = c_4^{\pm}, \quad (87)$$

$$-i t_{\pm}^{\pm} + i t_{\pm}^{\mp} = c_1^{\pm} e^{\xi k_y L} + c_2^{\pm} \frac{L}{\ell_1} e^{\xi k_y L}, \quad (88)$$

$$-t_{\pm}^{\pm} + t_{\pm}^{\mp} = c_3^{\pm} e^{-\xi k_y L}, \quad (89)$$

$$t_{\pm}^{\pm} + t_{\pm}^{\mp} = c_2^{\pm} e^{\xi k_y L}, \quad (90)$$

$$-i t_{\pm}^{\pm} - i t_{\pm}^{\mp} = -c_3^{\pm} \frac{L}{\ell_1} e^{-\xi k_y L} + c_4^{\pm} e^{-\xi k_y L}, \quad (91)$$

where $\ell_1 = \hbar v / \gamma_1$. Solving yields the transmission matrix

$$t = \begin{pmatrix} t_{+}^{+} & t_{+}^{-} \\ t_{-}^{+} & t_{-}^{-} \end{pmatrix} = \frac{2i}{2 + (L/\ell_1)^2 + 2 \cosh(2k_y L)} \times \begin{pmatrix} (L/\ell_1 - 2i) \cosh(k_y L) & -(L/\ell_1) \sinh(\xi k_y L) \\ (L/\ell_1) \sinh(\xi k_y L) & -(L/\ell_1 + 2i) \cosh(k_y L) \end{pmatrix}.$$

The transmission probability [168] is determined by the eigenvalues T_{\pm} of the product tt^{\dagger} :

$$T_{\pm} = \frac{1}{\cosh^2(\xi k_y L \mp k_c L)}, \quad (92)$$

$$k_c L = \ln \left[\frac{L}{2\ell_1} + \sqrt{1 + \left(\frac{L}{2\ell_1} \right)^2} \right], \quad (93)$$

The transmission coefficients T_{\pm} have the same form as the transmission in monolayer graphene $T = 1/\cosh^2(k_y L)$ [198] but shifted by the parameter k_c , as shown in figure 10.

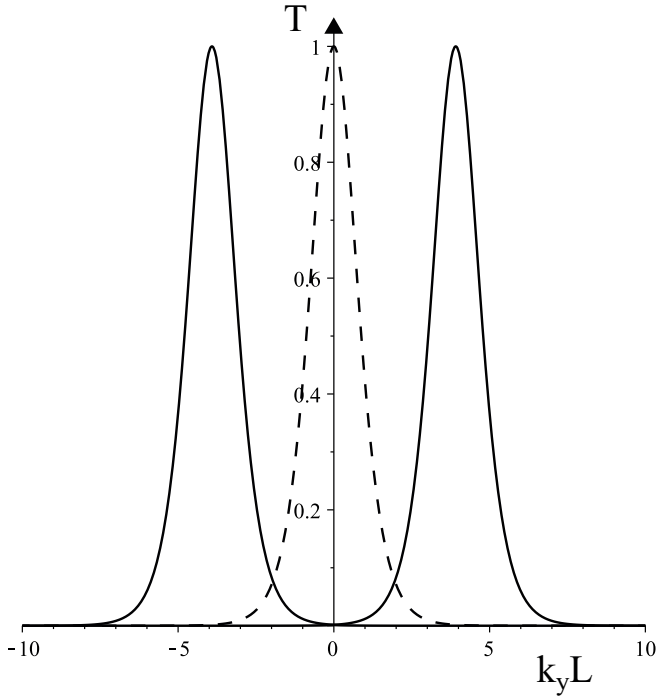


Figure 10. The transmission coefficients T_{\pm} of bilayer graphene (92) for $L = 50\ell_1$ [168] (solid lines). The transmission coefficient of monolayer graphene [198] is shown in the centre (dashed line). Reprinted with permission from [168]. Copyright 2007 by the American Physical Society.

The conductance G may be determined using the Landauer–Büttiker formula [199, 200]

$$G = \frac{g_v g_s e^2}{h} \text{Tr}(tt^\dagger), \quad (94)$$

where the factor of $g_v g_s$ accounts for valley and spin degeneracy. For a short, wide sample whose width W exceeds its length L , $W \gg L$, the transverse wavevector may be assumed to be continuous and

$$G = \frac{g_v g_s e^2}{h} \frac{W}{2\pi} \int_{-\infty}^{\infty} (T_+ + T_-) dk_y = \frac{2g_v g_s e^2}{h} \frac{W}{\pi L}. \quad (95)$$

Thus, the minimal conductivity $\sigma = GL/W = 8e^2/(\pi h)$ is twice as large as in the monolayer. In a similar way, it is possible to determine the Fano factor of shot noise which takes the same value $1/3$ [168] as in monolayer graphene [198]. Transmission via evanescent modes in graphene has been described as *pseudodiffusive* because the Fano factor takes the same value as in a diffusive metal [198].

4.3. Transport in disordered bilayer graphene

4.3.1. Conductivity. When the Fermi energy ε_F is much larger than the level broadening caused by the disorder potential, the system is not largely different from a conventional metal, and the conductivity is well described by Boltzmann transport theory. However, this approximation inevitably breaks down at the Dirac point, where even the issue of whether the system is metallic or insulating is nontrivial. To model electronic transport at the charge-neutrality point, we

need a refined approximation that properly includes the finite level broadening. Here, we present a conductivity calculation using the self-consistent Born approximation (SCBA) [163]. We define the Green's function as $G(\varepsilon) = (\varepsilon - \mathcal{H})^{-1}$. The Green's function averaged over the impurity configurations satisfies Dyson's equation

$$\langle G_{\alpha,\alpha'}(\varepsilon) \rangle = \delta_{\alpha,\alpha'} G_{\alpha}^{(0)}(\varepsilon) + G_{\alpha}^{(0)}(\varepsilon) \sum_{\alpha_1} \Sigma_{\alpha,\alpha_1}(\varepsilon) \langle G_{\alpha_1,\alpha'}(\varepsilon) \rangle, \quad (96)$$

where $\langle \rangle$ is an average over configurations of the disorder potential, α is an eigenstate of the ideal Hamiltonian \mathcal{H}_0 , and $G_{\alpha}^{(0)} = (\varepsilon - \varepsilon_{\alpha})^{-1}$, with ε_{α} being the eigenenergy of the state α in \mathcal{H}_0 . In SCBA, the self-energy is given by [201]

$$\Sigma_{\alpha,\alpha'}(\varepsilon) = \sum_{\alpha_1, \alpha'_1} \langle U_{\alpha,\alpha_1} U_{\alpha'_1,\alpha'} \rangle \langle G_{\alpha_1,\alpha'_1}(\varepsilon) \rangle. \quad (97)$$

Equations (96) and (97) need to be solved self-consistently. The conductivity is calculated using the Kubo formula,

$$\sigma(\varepsilon) = g_v g_s \frac{\hbar e^2}{2\pi \Omega} \times \text{ReTr} [v_x \langle G^R \rangle \tilde{v}_x^{\text{RA}} \langle G^A \rangle - v_x \langle G^R \rangle \tilde{v}_x^{\text{RR}} \langle G^R \rangle], \quad (98)$$

where $G^R = G(\varepsilon + i0)$ and $G^A = G(\varepsilon - i0)$ are retarded and advanced Green's functions, $v_x = \partial \mathcal{H}_0 / \partial p_x$ is the velocity operator, and $g_v g_s$ accounts for summation over valleys and spins. \tilde{v}_x^{RA} and \tilde{v}_x^{RR} are the velocity operators containing the vertex correction, defined by $\tilde{v}_x^{\text{RA}} = \tilde{v}_x(\varepsilon + i0, \varepsilon - i0)$ and $\tilde{v}_x^{\text{RR}} = \tilde{v}_x(\varepsilon + i0, \varepsilon + i0)$ with

$$\tilde{v}_x(\varepsilon, \varepsilon') = v_x + \langle U G(\varepsilon) \tilde{v}_x G(\varepsilon') U \rangle. \quad (99)$$

In SCBA, \tilde{v}_x should be calculated in the ladder approximation.

For the disorder potential, we assume a short-ranged potential within each valley,

$$U = \sum_i u_i \delta(\mathbf{r} - \mathbf{r}_i) \begin{pmatrix} 1 & 0 & 0 & 0 \\ 0 & 1 & 0 & 0 \\ 0 & 0 & 1 & 0 \\ 0 & 0 & 0 & 1 \end{pmatrix}. \quad (100)$$

and neglect intervalley scattering between K_+ and K_- . This situation is realized when the length scale of the scattering potential is larger than atomic scale but much shorter than the Fermi wave length. We assume an equal amount of positive and negative scatterers $u_i = \pm u$ and a total density of scatterers per unit area n_{imp} .

The SCBA formulation is applied to the low-energy Hamiltonian equation (38), with the trigonal warping effect due to γ_3 included [163]. Energy broadening due to the disorder potential is characterized by

$$\Gamma = \frac{\pi}{2} n_{\text{imp}} u^2 \frac{m^*}{2\pi \hbar}. \quad (101)$$

When $\Gamma \gtrsim \varepsilon_L$, i.e. the disorder is strong enough to smear out the fine band structure of the trigonal warping, we can approximately solve the SCBA equation in an analytic form.

The self-energy, equation (97), becomes diagonal with respect to index α and it is a constant,

$$\Sigma(\varepsilon + i0) \approx -i\Gamma. \quad (102)$$

Then, the conductivity at the Fermi energy ε is written as

$$\sigma(\varepsilon) \approx g_v g_s \frac{e^2}{\pi^2 \hbar} \frac{1}{2} \left[1 + \left(\frac{|\varepsilon|}{\Gamma} + \frac{\Gamma}{|\varepsilon|} \right) \arctan \frac{|\varepsilon|}{\Gamma} + \frac{4\pi\varepsilon_L}{\Gamma} \right]. \quad (103)$$

The third term in the square bracket arises from the vertex correction due to the trigonal warping effect, and ε_L is given by equation (42). For high energies $|\varepsilon| \gg \Gamma$, σ approximates as

$$\sigma(\varepsilon) \approx g_v g_s \frac{e^2}{\pi^2 \hbar} \frac{\pi}{4} \frac{|\varepsilon|}{\Gamma}, \quad (104)$$

which increases linearly with energy. The value at zero energy becomes

$$\sigma(0) = g_v g_s \frac{e^2}{\pi^2 \hbar} \left(1 + \frac{2\pi\varepsilon_L}{\Gamma} \right). \quad (105)$$

In the strong disorder regime $\Gamma \gg 2\pi\varepsilon_L$, the correction arising from trigonal warping vanishes and the conductivity approaches the universal value $g_v g_s e^2 / (\pi^2 \hbar)$ [163, 167] which is twice as large as that in monolayer graphene in the same approximation. In transport measurements of suspended bilayer graphene [161], the minimum conductivity was estimated to be about 10^{-4} S, which is close to $g_v g_s e^2 / (\pi^2 \hbar)$.

The 2×2 (two-band) model works well at low energies, but it is not expected to be valid in the strong disorder regime when mixing to higher energy bands is considerable. To see this, we numerically solved the SCBA equation for the original 4×4 (four-band) Hamiltonian. Figures 11(a) and (b) show the density of states (DOS) and conductivity, respectively, for several disorder strengths [202]. In (b) the results for the 2×2 model in equation (103) are expressed as broken curves. In (a), we observe that the DOS at zero energy is significantly enhanced because states at high energies are shifted towards the Dirac point by the disorder potential. However, the zero-energy conductivity barely shifts from that of the 2×2 model (equation (105)), even for strong disorder such as $\Gamma/\gamma_1 = 0.15$, where the DOS at zero energy becomes nearly twice as large as in the 2×2 model. For higher energies $|\varepsilon| > \Gamma$, the conductivity increases linearly with $|\varepsilon|$ in qualitative agreement with equation (103) of the 2×2 model, while the gradient is generally steeper. The conductivity has a small dip at the higher band edge around $|\varepsilon| \sim \gamma_1$, because the frequency of electron scattering is strongly enhanced by the higher band states.

The SCBA calculation was recently extended for long-range scatterers [203]. It was shown that the conductivity at zero energy is not universal but depends on the degree of disorder for scatterers with long-range potential, similar to monolayer graphene [204].

4.3.2. Localization effects. The SCBA does not take account of some quantum corrections, such as those included explicitly in weak localization. In graphene, the presence of spin-like degrees of freedom related to sublattices and valleys, as well

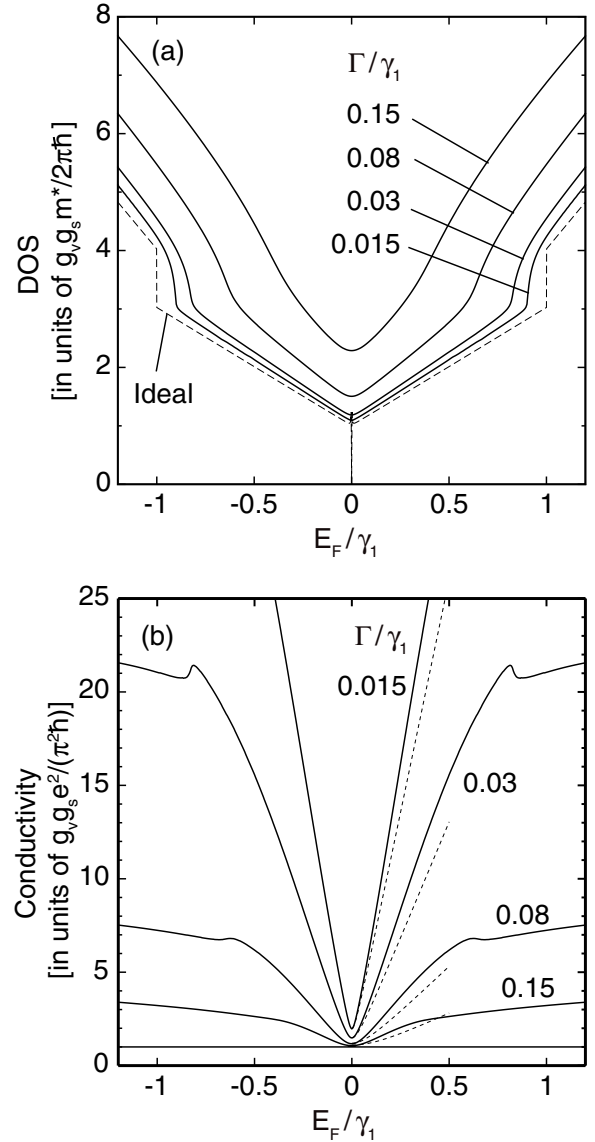


Figure 11. (a) Calculated density of states and (b) conductivity as a function of energy for different disorder strength Γ [202]. In (b), broken curves show the results of the low-energy two-band model, and the horizontal line indicates the universal conductivity $g_v g_s e^2 / (\pi^2 \hbar)$. Reprinted with permission from [202].

as real electronic spin itself, creates the possibility of a rich variety of quantum interference behaviour. Weak localization [205, 206] is a particularly useful probe because it is sensitive to elastic scattering that causes relaxation of the sublattice pseudospin and valley ‘spin’. In the absence of symmetry-breaking scattering processes, conservation of pseudospin in monolayer graphene tends to suppress backscattering [88, 207], and the interference of chiral electrons would be expected to result in antilocalization [208]. However, intravalley symmetry-breaking relaxes the pseudospin and suppresses anti-localization, while intervalley scattering tends to restore conventional weak localization [209–213], as observed experimentally [209, 214–219]. Nevertheless, anti-localization has been observed at high temperatures [218, 220] when the relative influence of symmetry-breaking disorder is diminished, and its presence has also been predicted at very

low temperatures [221–223] when spin–orbit coupling may influence the spin of the interfering electrons.

In bilayer graphene, the pseudospin turns twice as quickly in the graphene plane as in a monolayer, no suppression of backscattering is expected and the quantum correction should be conventional weak localization [212, 213, 224]. However, the relatively strong trigonal warping of the Fermi line around each valley (described in section 2.5) can suppress localization unless intervalley scattering is sufficiently strong [224]. Experimental observations confirmed this picture [159], and it was possible to determine the temperature and density dependence of relevant relaxation lengths by comparing with the predicted magnetoresistance formula [224].

Localization has also been studied for gapped bilayer graphene in the presence of interlayer potential asymmetry U [225]. It was shown that, as long as the disorder potential is long range and does not mix K_{\pm} valleys, gap opening inevitably causes electron delocalization somewhere between $U = 0$ and $U = \infty$, in accordance with the transition of quantum valley Hall conductivity, i.e. the opposite Hall conductivities associated with two valleys. This is an analogue of quantum Hall physics but can be controlled purely by an external electric field without any use of magnetic fields.

5. Optical properties

The electronic structure of bilayer graphene was probed by spectroscopic measurements in zero magnetic field [16, 55, 56, 79, 80, 129, 130], and also in high magnetic fields [78]. The optical absorption for perpendicularly incident light is described by the dynamical conductivity in an electric field parallel to the layers, in both symmetric bilayers [164, 226–228] and in the presence of an interlayer-asymmetry gap [227]. For symmetric bilayer graphene, this is explicitly estimated as [164, 226–228]

$$\begin{aligned} \text{Re } \sigma_{xx}(\omega) = & \frac{g_v g_s e^2}{16 \hbar} \left\{ \frac{\hbar\omega + 2\gamma_1}{\hbar\omega + \gamma_1} \theta(\hbar\omega - 2|\varepsilon_F|) \right. \\ & + \left(\frac{\gamma_1}{\hbar\omega} \right)^2 [\theta(\hbar\omega - \gamma_1) + \theta(\hbar\omega - \gamma_1 - 2|\varepsilon_F|)] \\ & + \frac{\hbar\omega - 2\gamma_1}{\hbar\omega - \gamma_1} \theta(\hbar\omega - 2\gamma_1) \\ & \left. + \gamma_1 \log \left[\frac{2|\varepsilon_F| + \gamma_1}{\gamma_1} \right] \delta(\hbar\omega - \gamma_1) \right\}, \quad (106) \end{aligned}$$

where ε_F is the Fermi energy and we assumed $|\varepsilon_F| < \gamma_1$. We label the four bands in order of descending energy as 1, 2, 3, 4. The first term in equation (106) represents absorption from band 2 to 3, the second from 2 to 4 or from 1 to 3, the third from 1 to 4, and the fourth from 3 to 4 or from 1 to 2. Figure 12(a) shows some examples of calculated dynamical conductivity $\text{Re } \sigma_{xx}(\omega)$ with several values of the Fermi energy [229]. The curve for $\varepsilon_F = 0$ has essentially no prominent structure except for a step-like increase corresponding to transitions from 2 to 4. With an increase in ε_F , a delta-function peak appears at $\hbar\omega = \gamma_1$, corresponding to allowed transitions 3 to 4.

In a magnetic field, an optical excitation by perpendicular incident light is only allowed between the Landau levels with n and $n \pm 1$ for arbitrary combinations of $\mu = H, L$ and

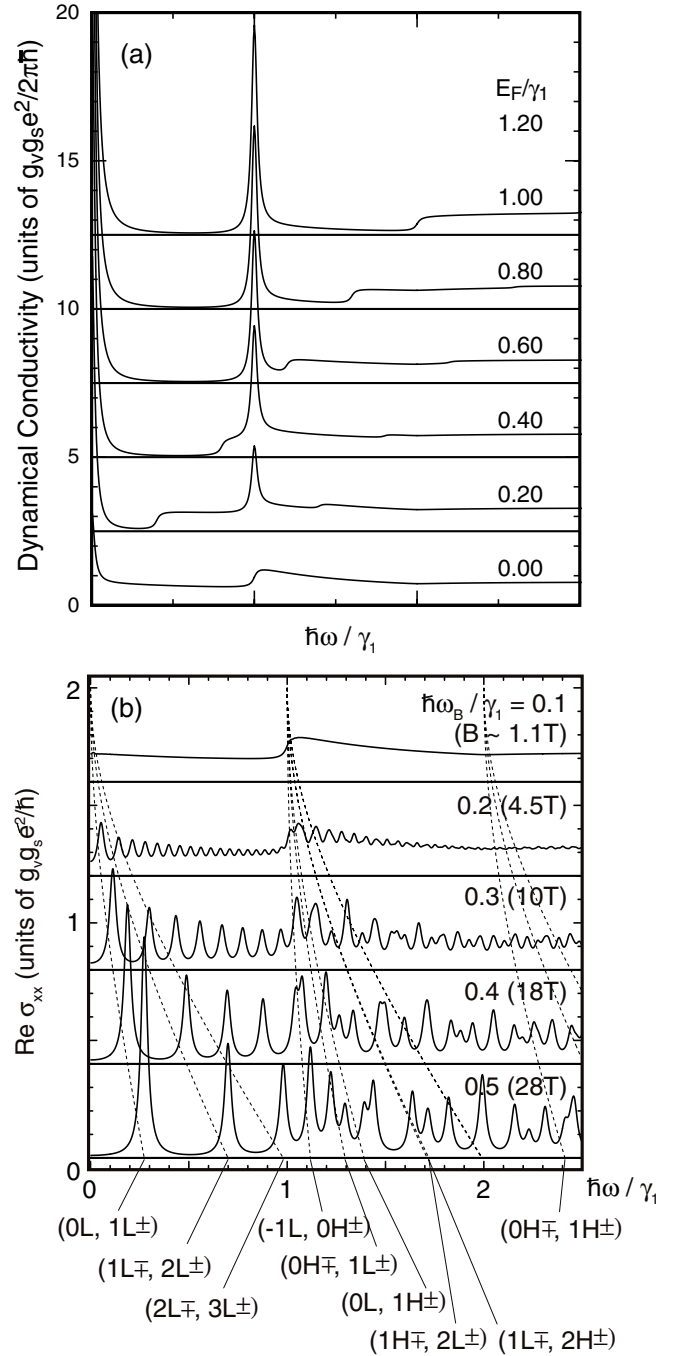


Figure 12. Interband part of the dynamical conductivity of bilayer graphene plotted against the frequency ω , in (a) zero magnetic field with different ε_F 's [229] (b) several magnetic fields with $\varepsilon_F = 0$ [230]. Dashed curves in (b) indicate the transition energies between several Landau levels. (a) Reprinted figure with permission from [229]. Copyright 2010 by the Physical Society of Japan. (b) Reprinted figure with permission from [230]. Copyright 2010 by the American Physical Society.

$s = \pm 1$, since the matrix element of the velocity operator v_x vanishes otherwise. Figure 12(b) shows some plots of $\text{Re } \sigma_{xx}(\omega)$ in magnetic fields at $\varepsilon_F = 0$ and zero temperature [230]. Dotted lines penetrating panels represent the transition energies between several specific Landau levels as a continuous function of $\hbar\omega_B$. Every peak position behaves as a linear function of $B \propto \hbar\omega_B^2$ in weak field but it switches over

to \sqrt{B} -dependence as the corresponding energy moves out of the parabolic band region. In small magnetic fields, the peak structure is smeared out into the zero-field curve more easily in the bilayer than in the monolayer, because the Landau level spacing is narrower in bilayer due to the finite band mass.

6. Orbital magnetism

Graphite and related materials exhibit a strong orbital diamagnetism which overcomes the Pauli spin paramagnetism. Theoretically the diamagnetic susceptibility was calculated for graphite [121, 231, 232], graphite intercalation compounds [233–236], as well as few-layer graphenes [237, 238]. In particular, monolayer graphene has a strong diamagnetic singularity at Dirac point, which is expressed as a Delta function in Fermi energy ε_F [121, 239–242]. In the bilayer, the singularity is relaxed by the modification of the band structure caused by the interlayer coupling as we will see in the following [234, 237].

When the spectrum is composed of discrete Landau levels ε_n , the thermodynamical potential is generally written as

$$\Omega = -\frac{1}{\beta} \frac{g_v g_s}{2\pi l_B^2} \sum_n \varphi(\varepsilon_n), \quad (107)$$

where $\beta = 1/k_B T$, $\varphi(\varepsilon) = \log[1 + e^{-\beta(\varepsilon - \zeta)}]$ with ζ being the chemical potential. In weak magnetic field, using the Euler–Maclaurin formula, the summation in n in equation (107) can be written as an integral in a continuous variable x with a residual term proportional to B^2 . The magnetization M and the magnetic susceptibility χ can be calculated by

$$M = -\left(\frac{\partial \Omega}{\partial B}\right)_\zeta, \quad \chi = \left.\frac{\partial M}{\partial B}\right|_{B=0} = -\left(\frac{\partial^2 \Omega}{\partial B^2}\right)_\zeta \Big|_{B=0}. \quad (108)$$

For monolayer graphene, the susceptibility is [121, 239]

$$\chi = -g_v g_s \frac{e^2 v^2}{6\pi c^2} \int_{-\infty}^{\infty} \left(-\frac{\partial f(\varepsilon)}{\partial \varepsilon}\right) d\varepsilon. \quad (109)$$

At zero temperature, it becomes a delta function in Fermi energy,

$$\chi(\varepsilon_F) = -g_v g_s \frac{e^2 v^2}{6\pi c^2} \delta(\varepsilon_F). \quad (110)$$

The delta-function susceptibility of monolayer graphene is strongly distorted by the interlayer coupling γ_1 . For the Hamiltonian of the symmetric bilayer graphene, the orbital susceptibility is calculated as [234, 237]

$$\chi(\varepsilon) = g_v g_s \frac{e^2 v^2}{4\pi c^2 \gamma_1} \theta(\gamma_1 - |\varepsilon|) \left(\log \frac{|\varepsilon|}{\gamma_1} + \frac{1}{3} \right). \quad (111)$$

The susceptibility diverges logarithmically at $\varepsilon_F = 0$, becomes slightly paramagnetic near $|\varepsilon_F| = \gamma_1$, and vanishes for $|\varepsilon_F| > \gamma_1$ where the higher subband enters. The integration of χ in equation (111) over the Fermi energy becomes $-g_v g_s e^2 v^2 / (3\pi c^2)$ independent of γ_1 , which is exactly twice as large as that of the monolayer graphene, equation (110).

The susceptibility was also calculated in the presence of interlayer asymmetry [243]. Figures 13(a) and (b) show the

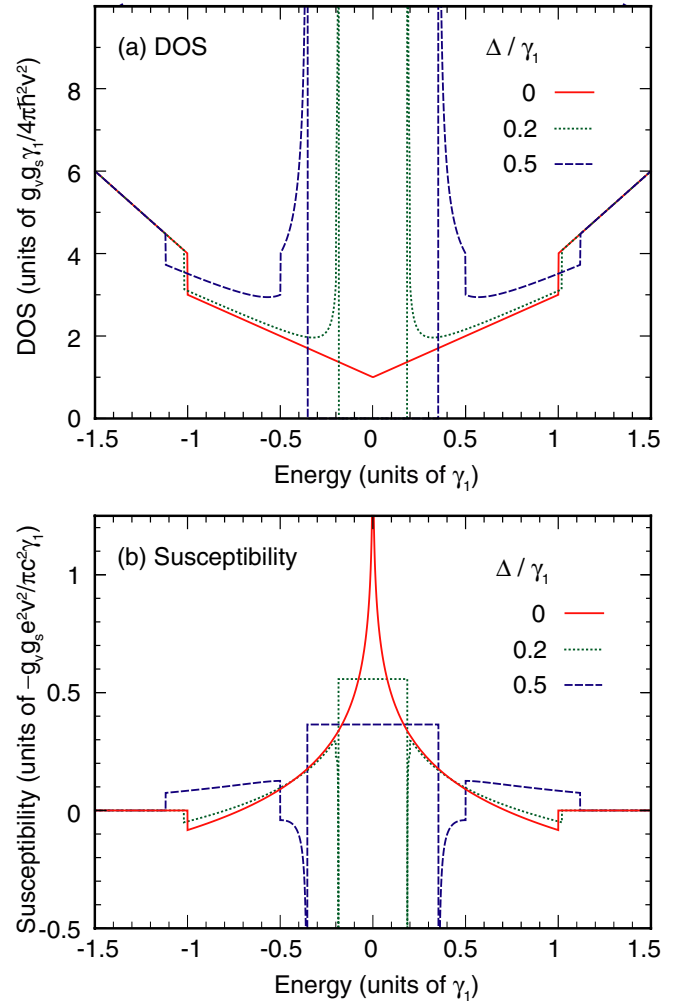


Figure 13. (a) Density of states, and (b) susceptibility of bilayer graphenes with the asymmetry gap $U/\gamma_1 = 0, 0.2$ and 0.5 [243]. In (b), the upward direction represents negative (i.e. diamagnetic) susceptibility. Reprinted figure with permission from [243]. Copyright 2010 by the American Physical Society.

density of states and the susceptibility, respectively, for bilayer graphene with $U = 0, 0.2$ and 0.5 . The susceptibility diverges in the paramagnetic direction at the band edges where the density of states also diverges. This huge paramagnetism can be interpreted as the Pauli paramagnetism induced by the valley pseudospin splitting and diverging density of states [244]. The susceptibility vanishes in the energy region where the higher subband enters.

7. Phonons and strain

7.1. The influence of strain on electrons in bilayer graphene

Deformation of a graphene sheet couples to the electronic system and modifies the low-energy Hamiltonian. In monolayer graphene, static changes in distance and angles of the atomic bonds can be described as effective scalar or vector potentials in the Dirac Hamiltonian [7, 245]. Bilayer graphene has extra degrees of freedom in deformation associated with the presence of two layers. It was shown that a band gap can

be opened by giving different distortions to the two layers or by pulling the two layers apart in the perpendicular direction [246–248].

Rather than producing a band gap, it has been predicted that homogeneous lateral strain in bilayer graphene can produce a change in topology of the band structure at low energies [249–251]. This deformation causes tight-binding parameters γ_0 and γ_3 to become dependent on the hopping direction and produces an additional term in the low-energy two-band Hamiltonian (38)

$$\hat{h}_s = \begin{pmatrix} 0 & w \\ w^* & 0 \end{pmatrix}, \quad (112)$$

where parameter $w = |w|e^{i\theta}$ depends on the microscopic details of the deformation; it is non-zero only when the role of skew interlayer coupling γ_3 is taken into account [249]. It is estimated that 1% strain would give $|w| \sim 6$ meV [249]. Taken with the quadratic term \hat{h}_0 in the Hamiltonian (38), the low-energy bands with energy $E = \pm\varepsilon_1$ are given by

$$\varepsilon_1^2 = |w|^2 - \frac{|w|p^2}{m} \cos(2\varphi + \theta) + \left(\frac{p^2}{2m}\right)^2. \quad (113)$$

This describes a Lifshitz transition at energy $\varepsilon_L = |w|$, below which there are two Dirac points in the vicinity of each Brillouin zone corner [249–251], centred at momentum $p \approx \sqrt{2m|w|} = \sqrt{|w|\gamma_1}/v$ and angles $\varphi = -\theta/2$ and $\varphi = \pi - \theta/2$. In general, there should be an interplay between terms \hat{h}_s , equation (112), and \hat{h}_w , equation (38), leading to the possibility of employing strain to annihilate two Dirac points and, thus, change the low-energy topology of the bands from four to two Dirac points [249].

The presence of two Dirac points would cause zero-energy Landau levels to be eightfold degenerate; an experimental signature of this state is predicted to be the persistence of filling factor $\nu = \pm 4$ in the low-field quantum Hall effect [249]. This contrasts with the Lifshitz transition that would occur in the presence of parameter γ_3 without strain when there are four Dirac points, section 2.5, giving a degeneracy of sixteen and $\nu = \pm 8$ at low fields. In both cases, Berry phase 2π is conserved: two Dirac cones with Berry phase π each [249] or four Dirac cones with three of π and one of $-\pi$ [12, 94]. It has also been predicted that the presence of the Lifshitz transition will be noticeable in the low-energy conductivity at zero magnetic field [163, 169], and the particular case of two Dirac points in the presence of strain has also recently been analysed [252]. Note that the effect of lateral strain on the low-energy topology of the band structure is qualitatively similar to that of a gapless nematic phase which possibly arises as the result of electron–electron interactions in bilayer graphene [253–256].

7.2. Phonons in bilayer graphene

Raman spectroscopy has been a valuable tool in probing the behaviour of phonons in graphite [257] and it may be used to determine the number of layers in multilayer graphene [258], differentiating between monolayer and bilayer. For an in-depth

review of Raman spectroscopy of graphene including bilayer graphene see, for example, [259, 260]. The phonon spectrum of monolayer graphene has been calculated using a tight-binding force-constant model with parameters fit to Raman data [261], and with density-functional theory [262–265]. There are three acoustic (A) and three optical (O) branches consisting of longitudinal (L) and transverse (T) in-plane modes as well as out-of-plane (Z) modes. At the zone centre (the Γ point), the TA and LA modes display linear dispersion $\omega \sim q$ but the ZA mode is quadratic $\omega \sim q^2$. The ZO mode is at ~ 890 cm^{−1} [262, 264], and the LO and TO modes are degenerate (at ~ 1600 cm^{−1}). At the K point, the ZA and ZO modes (~ 540 cm^{−1}) and the LA and LO modes (~ 1240 cm^{−1}) are degenerate, with TA modes at ~ 1000 cm^{−1} and TO at ~ 1300 cm^{−1}. For undoped graphene, owing to strong electron–phonon coupling, the highest optical modes at the Γ and K point (i.e. the LO mode at the Γ point and the TO mode at the K point) display Kohn anomalies [266–268] whereby the phonon dispersion $\omega(q)$ has an almost linear slope as observed, for example, in inelastic x-ray measurements of graphite [263, 268]. As graphene is a unique system in which the electron or hole concentration can be tuned by an external gate voltage, it was realized [269, 270] that the change in electron density would also influence the behaviour of the optical phonons through electron–phonon coupling and, in particular, a logarithmic singularity in their dispersion was predicted [269] when the Fermi energy ε_F is half of the energy of the optical phonon $|\varepsilon_F| = \hbar\omega/2$. Subsequently, such a tuning of phonon frequency and bandwidth by adjusting the electronic density was observed in monolayer graphene through Raman spectroscopy [271, 272].

The behaviour of phonons in bilayer graphene has been observed experimentally through Raman spectroscopy [76, 77, 273–279] and infrared spectroscopy [280, 281], with particular focus on optical phonon anomalies and the influence of gating. Generally, the phonon spectrum of bilayer graphene, which has been calculated using density-functional theory [282, 283] and force-constant models [284, 285], is similar to that of monolayer. Near the Γ point there are additional low-frequency modes. There is a doubly degenerate rigid shear mode at ~ 30 cm^{−1} [284, 285] observed through Raman spectroscopy [278] and an optical mode at ~ 90 cm^{−1} which arises from relative motion of the layers in the vertical direction (perpendicular to the layer plane), known as a layer-breathing mode [286] and observed through Raman spectroscopy [279]. At the Γ point, interlayer coupling causes the LO/TO modes to split into two doubly degenerate branches where the higher (lower) frequency branch corresponds to symmetric ‘in-phase’ (antisymmetric ‘out-of-phase’) relative motion of atoms on the two layers (in the in-plane direction). Analogously to the monolayer, it was predicted that these optical phonons would be affected by electron–phonon coupling, with a logarithmic singularity in the dispersion of the symmetric modes when the Fermi energy ε_F is equal to half of the optical phonon frequency [287], and hybridization of the symmetric and antisymmetric modes in the presence of interlayer potential asymmetry [288, 289]. Experimentally, this anomalous phonon dispersion has been observed through Raman spectroscopy [77, 273–276]

including the evolution of two distinct components in the Raman G band for non-zero interlayer asymmetry [274–276]. The Raman spectrum has also been studied for bilayer graphene in the presence of Landau levels in a magnetic field [287, 290].

7.3. Optical phonon anomaly

In the following, we describe the anomalous optical phonon spectrum in bilayer graphene taking into account electron–phonon coupling [287, 288]. Theoretically, it was shown that a continuum model works well in describing long-wavelength acoustic phonons [245] and optical phonons [291] in graphene, and this theory was extended to bilayer graphene [287, 288]. An optical phonon on the one graphene layer is represented by the relative displacement of two sublattice atoms A and B as

$$\mathbf{u}(\mathbf{r}) = \sum_{\mathbf{q}, \mu} \sqrt{\frac{\hbar}{4NM\omega_0}} (b_{\mathbf{q}, \mu} + b_{-\mathbf{q}, \mu}^\dagger) \mathbf{e}_\mu(\mathbf{q}) e^{i\mathbf{q} \cdot \mathbf{r}}, \quad (114)$$

where N is the number of unit cells, M is the mass of a carbon atom, ω_0 is the phonon frequency at the Γ point, $\mathbf{q} = (q_x, q_y)$ is the wave vector, and $b_{\mathbf{q}, \mu}$ and $b_{\mathbf{q}, \mu}^\dagger$ are the creation and destruction operators, respectively. The index μ represents the modes (t for transverse and l for longitudinal), and corresponding unit vectors are defined by $\vec{e}_l = i\mathbf{q}/|\mathbf{q}|$ and $\vec{e}_t = i\hat{z} \times \mathbf{q}/|\mathbf{q}|$.

The Hamiltonian of optical phonons is written as

$$\mathcal{H}_{\text{ph}} = \sum_{\mathbf{q}, \mu} \hbar\omega_0 \left(b_{\mathbf{q}, \mu}^\dagger b_{\mathbf{q}, \mu} + \frac{1}{2} \right), \quad (115)$$

and the interaction with an electron at the K_+ point is

$$\mathcal{H}_{\text{int}}^K = -\sqrt{2} \frac{\beta \hbar v}{a_{\text{CC}}^2} [\sigma_x u_y(\mathbf{r}) - \sigma_y u_x(\mathbf{r})], \quad (116)$$

where the Pauli matrix σ_i works on the space of (ϕ_{A1}, ϕ_{B1}) for the phonon on layer 1, and (ϕ_{A2}, ϕ_{B2}) for layer 2. The dimensionless parameter β is related to the dependence of the hopping integral on the interatomic distance, and is defined by $\beta = -d \log \gamma_0 / d \log a_{\text{CC}}$. We usually expect $\beta \sim 2$. The strength of the electron–phonon interaction is characterized by a dimensionless parameter

$$\lambda = \frac{g_v g_s}{4} \frac{36\sqrt{3}}{\pi} \frac{\hbar}{2Ma^2 \hbar\omega_0} \left(\frac{\beta}{2} \right)^2. \quad (117)$$

For $M = 1.993 \times 10^{23}$ g and $\hbar\omega_0 = 0.196$ eV (corresponding to 1583 cm^{-1}), we have $\lambda \approx 3 \times 10^{-3} (\beta/2)^2$. For the K_- point, the interaction Hamiltonian is obtained by replacing σ_i with $-\sigma_i^*$.

The Green's function of an optical phonon is given by a 2×2 matrix associated with phonons on layers 1 and 2. This is written as

$$\begin{aligned} \hat{D}(\mathbf{q}, \omega) &= \frac{2\hbar\omega_0}{(\hbar\omega)^2 - (\hbar\omega_0)^2 - 2\hbar\omega_0 \hat{\Pi}(\mathbf{q}, \omega)} \\ &\approx \frac{1}{\hbar\omega - \hbar\omega_0 - \hat{\Pi}(\mathbf{q}, \omega_0)}, \end{aligned} \quad (118)$$

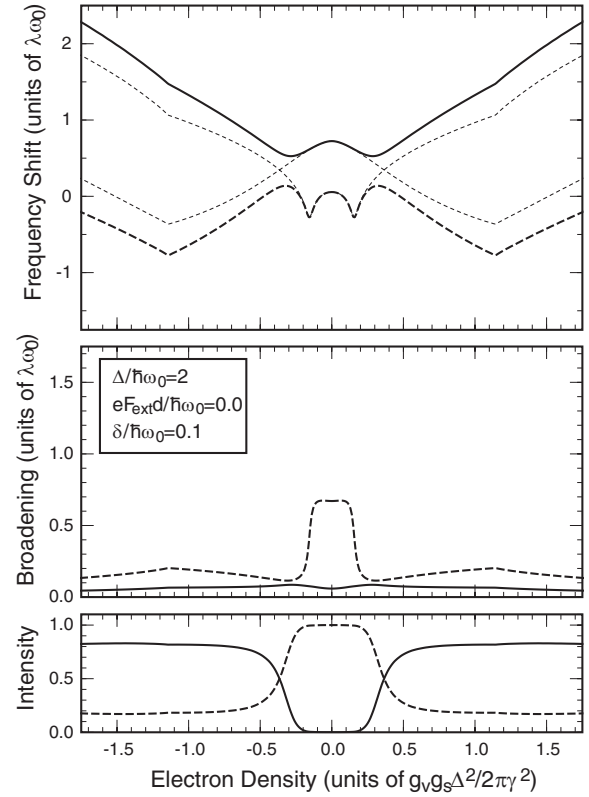


Figure 14. The frequency shift (top panel), broadening (middle panel), and the spectral intensity (bottom panel) of the symmetric component for an optical phonon in a bilayer graphene [288]. Solid and dashed lines denote the high- and low-frequency modes, respectively, and the thin dotted lines in the top panel show the frequencies for symmetric and antisymmetric modes calculated without inclusion of their mixing. Reprinted figure with permission from [288]. Copyright 2009 by the Physical Society of Japan.

where $\hat{\Pi}(\mathbf{q}, \omega)$ is the phonon's self-energy, and the near-equality in the second line stands because the self-energy is much smaller than $\hbar\omega_0$. Then, the eigenmodes are given by eigenvectors $|u\rangle$ of $\text{Re} \hat{\Pi}(\mathbf{q}, \omega_0)$, and the frequency shift and broadening are obtained as the real and imaginary part of $\langle u | \hat{\Pi}(\mathbf{q}, \omega_0) | u \rangle$.

In symmetric bilayer graphene (i.e. no interlayer potential difference), eigenmodes are always classified into symmetric and antisymmetric modes in which the displacement of the top and bottom layers is given by (\mathbf{u}, \mathbf{u}) for the former, and $(\mathbf{u}, -\mathbf{u})$ for the latter. The symmetric mode causes interband transitions between the conduction band and valence band, while the antisymmetric mode contributes to the transitions between two conduction bands (or between two valence bands). The potential difference between two layers gives rise to hybridization of symmetric and antisymmetric modes [287].

Figures 14(a) and (b) show the calculated frequency shift and broadening, respectively, as a function of electron density n_s [288]. Here we take $\hbar\omega_0 = \gamma_1/2$, and introduce a phenomenological broadening factor of $0.1\hbar\omega_0$. We assume that n_s is changed by the gate voltage, and appropriately take account of the band deformation due to the interlayer potential difference when $n_s \neq 0$, with the self-consistent screening effect included. The thin dotted lines in the top

panel in figure 14(a) indicate the frequencies for symmetric and antisymmetric modes calculated without inclusion of their mixing. The lower and higher branches exactly coincide with symmetric and asymmetric modes at $n_s = 0$ where the mixing is absent. The dip at the symmetric mode occurs when $\hbar\omega_0 = 2\varepsilon_F$, i.e. the interband transition excites a valence electron exactly to the Fermi surface. The coupling between symmetric and antisymmetric modes arises when $n_s \neq 0$, and makes an anti-crossing at the intersection.

8. Electronic interactions

Generally speaking, the low-energy behaviour of electrons in bilayer graphene is well described by the tight-binding model without the need to explicitly incorporate electron–electron interaction effects. Coulomb screening and collective excitations have been described in a number of theoretical papers [152, 292–300] and the importance of interaction effects in a bilayer under external gating [293, 301–307] has been stressed. Interaction effects should also be important in the presence of a magnetic field or at very low carrier density, particularly in clean samples.

Bilayer graphene has quadratic bands which touch at low energies resulting in a non-vanishing density of state and it has been predicted to be unstable to electron–electron interactions at half filling. Trigonal warping tends to cut off infrared singularities and, thus, finite coupling strength is generally required to realize correlated ground states; if trigonal warping is neglected, then arbitrarily weak interactions are sufficient. Since bilayer graphene possesses pseudospin (i.e. which layer) and valley degrees of freedom, in addition to real electron spin, it is possible to imagine a number of different broken symmetry states that could prevail depending on model details and parameter values. Suggestions include a ferromagnetic [308], layer antiferromagnetic [14, 87, 309–312], ferroelectric [311, 313] or a charge density wave state [314]; topologically non-trivial phases with bulk gaps and gapless edge excitations such as an anomalous quantum Hall state [87, 311, 315, 316] or a quantum spin Hall state [87, 311] (also called a spin flux state [256]); or a gapless nematic phase [317, 253–256].

Insulating states contribute a term proportional to σ_z in the two-band Hamiltonian (38) with its sign corresponding to the distribution of layer, valley and spin degrees of freedom, indicated in figure 15, as manifest in their spin- and valley-dependent Hall conductivities [14, 87, 311]. Note that the quantum spin Hall state produces a term equivalent to that of intrinsic spin–orbit coupling, equation (46), which describes a topological insulator state [99, 110, 111]. By way of contrast, the gapless nematic phase has a qualitatively similar effect on the spectrum of bilayer graphene as lateral strain [249], described in section 7, producing an additional term in the two-band Hamiltonian of the form of equation (112), with parameter w taking the role of an order parameter.

Experiments on suspended bilayer graphene devices have found evidence for correlated states at very low density and zero magnetic field [318–324]. Conductivity measurements of double-gate devices [318] observed a non-monotonic dependence of the resistance on electric field

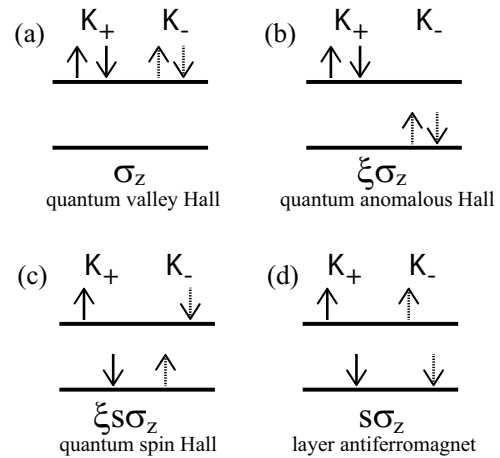


Figure 15. Schematic of the distribution of spin, valley and layer degrees of freedom in candidates for spontaneous gapped states in bilayer graphene [14, 87, 311]. They each contribute a term proportional to σ_z in the two-band Hamiltonian (38), with its sign depending on the valley $\xi = \pm 1$ and spin $s = \pm 1$ orientation. Arrows indicate spin orientation, located at valley K_+ (solid) or K_- (dashed) and on different layers (top or bottom) of a state at the top of the valence band.

cumulating in a non-divergent resistance at zero field while compressibility measurements of single-gate devices [319] found an incompressible region near the charge-neutrality point. These measurements were interpreted as being consistent with either the anomalous quantum Hall state, in which the separate layers of the device are valley polarized, or the gapless nematic phase.

Subsequently, conductivity measurements on single-gate devices [320] observed a weak temperature dependence of the width of the conductivity minimum near zero carrier density, suggesting a suppressed density of states as compared with that expected for a parabolic dispersion, as well as particularly robust cyclotron gaps at filling factor $\nu = \pm 4$, observations attributed to the presence of the nematic phase.

However, other experiments [321–324] observed insulating states indicating the formation of ordered phases with energy gaps of about 2 meV. There was evidence for the existence of edge states in one of these experiment [321], but not in the others [322–324], and the latter observations including their response to perpendicular electric field [322, 323] and tilted magnetic field [324] were seen as being consistent with a layer antiferromagnetic state, in which the separate layers of the device are spin polarized, figure 15(d). At present, there appear to be contradicting experimental and theoretical results, but it should be noted that renormalization group studies [325, 255, 256] have highlighted the sensitivity of the phase diagram of bilayer graphene to microscopic details.

In the absence of interactions, the low-energy Landau level spectrum of bilayer graphene [9] consists of a series of fourfold (spin and valley) degenerate levels with an eightfold-degenerate level at zero energy, as described in section 2.10. The resulting Hall conductivity consists of a series of plateaus at conventional integer positions of $4e^2/h$, but with a double-sized step of $8e^2/h$ across zero density [8]. Interaction effects are expected to lift the level degeneracy of quantum Hall

ferromagnet states at integer filling factors [326–331]. In fact, an insulating state at filling factor $\nu = 0$ and complete splitting of the eightfold-degenerate level at zero energy have been observed with quantum states at filling factors $\nu = 0, \pm 1, \pm 2$ and ± 3 in high-mobility suspended bilayer graphene at low fields (with all states resolved at $B = 3$ T) [161, 332] and in samples on silicon substrates at high fields, typically above 20 T [333, 334].

The fractional quantum Hall effect has been observed recently in monolayer graphene, both in suspended samples [335, 336] and graphene on boron nitride [337], and there is also evidence for it in bilayer graphene [338]. Strongly correlated states at fractional filling factors and the prospect of tuning their properties have been the focus of recent theoretical attention [339–343]. Clearly, the nature of the electronic properties of bilayer graphene in high-mobility samples is a complicated problem, and it is likely to be an area of further intense experimental and theoretical investigation in the following years.

9. Summary

This review focused on the single-particle theory of electrons in bilayer graphene, in the shape of the tight-binding model and the related low-energy effective Hamiltonian. Bilayer graphene has two unique properties: massive chiral quasiparticles in two parabolic bands which touch at zero energy, and the possibility to control an infrared gap between these low-energy bands by applying an external gate potential. These features have a dramatic impact on many physical properties of bilayer graphene including some described here: optical and transport properties, orbital magnetism, phonons and strain. A number of topics were not covered here in great detail or at all; we refer the reader to relevant detailed reviews of graphene including electronic transport [176, 177], electronic and photonic devices [344], scanning tunnelling microscopy [345], Raman spectroscopy [259, 260], magnetism [346], spintronics and pseudospintronics [347], Andreev reflection at the interface with a superconductor and Klein tunnelling [348], growth and applications [21], and the properties of graphene in general [7, 349]. Finally, although the central features of the single-particle theory are already established, the same cannot be said of the influence of electronic interactions, which is likely to remain a subject of intense research, both theoretical and experimental, in the near future at least.

Acknowledgments

The authors are grateful to colleagues for fruitful collaboration in graphene research, in particular T Ando and V I Fal'ko, and they acknowledge funding by the JST-EPSRC Japan-UK Cooperative Programme Grant EP/H025804/1.

References

- [1] Novoselov K S, Geim A K, Morozov S V, Jiang D, Zhang Y, Dubonos S V, Grigorieva I V and Firsov A A 2004 *Science* **306** 666
- [2] Novoselov K S, Geim A K, Morozov S V, Jiang D, Katsnelson M I, Grigorieva I V, Dubonos S V and Firsov A A 2005 *Nature* **438** 197
- [3] Zhang Y B, Tan Y W, Stormer H L and Kim P 2005 *Nature* **438** 201
- [4] DiVincenzo D P and Mele E J 1984 *Phys. Rev. B* **29** 1685
- [5] Semenoff G W 1984 *Phys. Rev. Lett.* **53** 2449
- [6] Haldane F D M 1988 *Phys. Rev. Lett.* **61** 2015
- [7] Castro Neto A H, Guinea F, Peres N M R, Novoselov K S and Geim A K 2009 *Rev. Mod. Phys.* **81** 109
- [8] Novoselov K S, McCann E, Morozov S V, Fal'ko V I, Katsnelson M I, Zeitler U, Jiang D, Schedin F and Geim A K 2006 *Nature Phys.* **2** 177
- [9] McCann E and Fal'ko V I 2006 *Phys. Rev. Lett.* **96** 086805
- [10] Guinea F, Castro Neto A H and Peres N M R 2006 *Phys. Rev. B* **73** 245426
- [11] Koshino M and Ando T 2007 *Phys. Rev. B* **76** 085425
- [12] Mañes J L, Guinea F and Vozmediano M A H 2007 *Phys. Rev. B* **75** 155424
- [13] Nakamura M and Hirasawa L 2008 *Phys. Rev. B* **77** 045429
- [14] Min H, Borghi G, Polini M and MacDonald A H 2008 *Phys. Rev. B* **77** 041407
- [15] Min H and MacDonald A H 2008 *Phys. Rev. B* **77** 155416
- [16] Ohta T, Bostwick A, Seyller T, Horn K and Rotenberg E 2006 *Science* **313** 951
- [17] McCann E 2006 *Phys. Rev. B* **74** 161403(R)
- [18] Min H, Sahu B R, Banerjee S K and MacDonald A H 2007 *Phys. Rev. B* **75** 155115
- [19] Oostinga J B, Heersche H B, Liu X, Morpurgo A F and Vandersypen L M K 2007 *Nature Mater.* **7** 151
- [20] Castro E V, Novoselov K S, Morozov S V, Peres N M R, Lopes dos Santos J M B, Nilsson J, Guinea F, Geim A K and Castro Neto A H 2007 *Phys. Rev. Lett.* **99** 216802
- [21] Novoselov K S, Fal'ko V I, Colombo L, Gellert P R, Schwab M G and Kim K 2012 *Nature* **490** 192
- [22] Dean C R *et al* 2010 *Nature Nanotechnol.* **5** 722
- [23] Ghosh S, Bao W, Nika D L, Subrina S, Pokatilov E P, Lau C N and Balandin A A 2010 *Nature Mater.* **9** 555
- [24] Balandin A A 2011 *Nature Mater.* **10** 569
- [25] Neek-Amal M and Peeters F M 2010 *Phys. Rev. B* **81** 235421
- [26] Zhang Y Y, Wang C M, Cheng Y and Xiang Y 2011 *Carbon* **49** 4511
- [27] Nair R R, Blake P, Grigorenko A N, Novoselov K S, Booth T J, Stauber T, Peres N M R and Geim A K 2008 *Science* **320** 1308
- [28] Bunch J S, Verbridge S S, Alden J S, an der Zande A M, Parpia J M, Craighead H G and McEuen P L 2008 *Nano Lett.* **8** 2458
- [29] Elias D C *et al* 2009 *Science* **323** 610
- [30] Bae S *et al* 2010 *Nature Nanotechnol.* **5** 574
- [31] Xia F, Farmer D B, Lin Y-M and Avouris P 2010 *Nano Lett.* **10** 715
- [32] Wang C-R, Lu W-S, Hao L, Lee W-L, Lee T-K, Lin F, Cheng I-C and Chen J-Z 2011 *Phys. Rev. Lett.* **107** 186602
- [33] Yan H, Li X, Chandra B, Tulevski G, Wu Y, Freitag M, Zhu W, Avouris P and Xia F 2012 *Nature Nanotechnol.* **7** 330
- [34] Yan J, Kim M-H, Elle J A, Sushkov A B, Jenkins G S, Milchberg H M, Fuhrer M S and Drew H D 2012 *Nature Nanotechnol.* **7** 472
- [35] Sugawara K, Kanetani K, Sato T and Takahashi T 2011 *AIP Adv.* **1** 022103
- [36] Kanetani K, Sugawara K, Sato T, Shimizu R, Iwaya K, Hitosugi T and Takahashia T 2012 *Proc. Natl Acad. Sci.* **109** 19610
- [37] Gong L, Young R J, Kinloch I A, Riaz I, Jalil R and Novoselov K S 2012 *ACS Nano* **6** 2086
- [38] Young R J, Kinloch I A, Gong L and Novoselov K S 2012 *Compos. Sci. Technol.* **72** 1459

- [39] Goossens A M, Driessen S C M, Baart T A, Watanabe K, Taniguchi T and Vandersypen L M K 2012 *Nano Lett.* **12** 4656
- [40] Liu Z, Suenaga K, Harris P J F and Iijima S 2009 *Phys. Rev. Lett.* **102** 015501
- [41] Lopes dos Santos J M B, Peres N M R and Castro Neto A H 2007 *Phys. Rev. Lett.* **99** 256802
- [42] Berger C *et al* 2006 *Science* **312** 1191
- [43] Hass J, Varchon F, Millán-Otoya J E, Sprinkle M, Sharma N, de Heer W A, Berger C, First P N, Magaud L and Conrad E H 2008 *Phys. Rev. Lett.* **100** 125504
- [44] Mele E J 2010 *Phys. Rev. B* **81** 161405
- [45] Li G, Luican A, Lopes dos Santos J M B, Castro Neto A H, Reina A, Kong J and Andrei E Y 2010 *Nature Phys.* **6** 109
- [46] Luican A, Li G, Reina A, Kong J, Nair R R, Novoselov K S, Geim A K and Andrei E Y 2011 *Phys. Rev. Lett.* **106** 126802
- [47] Schmidt H, Lüdtke T, Barthold P, McCann E, Fal'ko V I and Haug R J 2008 *Appl. Phys. Lett.* **93** 172108
- [48] Ni Z, Wang Y, Yu T, You Y and Shen Z 2008 *Phys. Rev. B* **77** 235403
- [49] Min H, Biströtzer R, Su J-J and MacDonald A H 2008 *Phys. Rev. B* **78** 121401
- [50] Kharitonov M Y and Efetov K B 2008 *Phys. Rev. B* **78** 241401
- [51] Schmidt H, Lüdtke T, Barthold P and Haug R J 2010 *Physica E* **42** 699
- [52] Ponomarenko L A *et al* 2011 *Nature Phys.* **7** 958
- [53] Saito R, Dresselhaus M S and Dresselhaus G 1998 *Physical Properties of Carbon Nanotubes* (London: Imperial College Press)
- [54] Nilsson J, Castro Neto A H, Guinea F and Peres N M R 2008 *Phys. Rev. B* **78** 045405
- [55] Zhang L M, Li Z Q, Basov D N, Fogler M M, Hao Z and Martin M C 2008 *Phys. Rev. B* **78** 235408
- [56] Li Z Q, Henriksen E A, Jiang Z, Hao Z, Martin M C, Kim P, Stormer H L and Basov D N 2009 *Phys. Rev. Lett.* **102** 037403
- [57] Latil S and Henrard L 2006 *Phys. Rev. Lett.* **97** 036803
- [58] Koshino M and McCann E 2010 *Phys. Rev. B* **81** 115315
- [59] Ashcroft N W and Mermin N D 1976 *Solid-State Physics* (Belmont: Brooks/Cole)
- [60] McCann E 2012 *Graphene Nanoelectronics: Metrology, Synthesis, Properties and Applications* ed H Raza (Berlin: Springer) pp 237–75
- [61] Partoens B and Peeters F M 2006 *Phys. Rev. B* **74** 075404
- [62] Mucha-Kruczyński M, Tsyplatyev O, Grishin A, McCann E, Fal'ko V I, Bostwick A and Rotenberg E 2008 *Phys. Rev. B* **77** 195403
- [63] Mucha-Kruczyński M, McCann E and Fal'ko V I 2010 *Semicond. Sci. Technol.* **25** 033001
- [64] Slonczewski J C and Weiss P R 1958 *Phys. Rev.* **109** 272
- [65] McClure J W 1957 *Phys. Rev.* **108** 612
- [66] McClure J W 1960 *Phys. Rev.* **119** 606
- [67] Dresselhaus M S and Dresselhaus G 2002 *Adv. Phys.* **51** 1
- [68] Aoki M and Amawashi H 2007 *Solid State Commun.* **142** 123
- [69] McCann E, Abergel D S L and Fal'ko V I 2007 *Solid State Commun.* **143** 110
- [70] Guinea F, Castro Neto A H and Peres N M R 2007 *Solid State Commun.* **143** 116
- [71] McCann E, Abergel D S L and Fal'ko V I 2007 *Eur. Phys. J. Spec. Top.* **148** 15
- [72] Guinea F, Castro Neto A H and Peres N M R 2007 *Eur. Phys. J. Spec. Top.* **148** 117
- [73] Gava P, Lazzeri M, Saitta A M and Mauri F 2009 *Phys. Rev. B* **79** 165431
- [74] Boukhalov D W and Katsnelson M I 2008 *Phys. Rev. B* **78** 085413
- [75] Mucha-Kruczyński M, Abergel D S L, McCann E and Fal'ko V I 2009 *J. Phys.: Condens. Matter* **21** 344206
- [76] Malard L M, Nilsson J, Elias D C, Brant J C, Plentz F, Alves E S, Castro Neto A H and Pimenta M A 2007 *Phys. Rev. B* **76** 201401(R)
- [77] Das A, Chakraborty B, Piscanec S, Pisana S, Sood A K and Ferrari A C 2009 *Phys. Rev. B* **79** 155417
- [78] Henriksen E A, Jiang Z, Tung L-C, Schwartz M E, Takita M, Wang Y-J, Kim P and Stormer H L 2008 *Phys. Rev. Lett.* **100** 087403
- [79] Kuzmenko A B, van Heumen E, van der Marel D, Lerch P, Blake P, Novoselov K S and Geim A K 2009 *Phys. Rev. B* **79** 115441
- [80] Kuzmenko A B, Crassee I, van der Marel D, Blake P and Novoselov K S 2009 *Phys. Rev. B* **80** 165406
- [81] Mak K F, Sfeir M Y, Misewich J A and Heinz T F 2010 *Proc. Natl Acad. Sci.* **107** 14999
- [82] Taychatanapat T, Watanabe K, Taniguchi T and Jarillo-Herrero P 2011 *Nature Phys.* **7** 621
- [83] Trickey S B, Müller-Plathe F, Diercksen G H F and Boettger J C 1992 *Phys. Rev. B* **45** 4460
- [84] Koshino M and McCann E 2009 *Phys. Rev. B* **80** 165409
- [85] Zhang F, Sahu S, Min H and MacDonald A H 2010 *Phys. Rev. B* **82** 035409
- [86] Berry M V 1984 *Proc. R. Soc. Lond. A* **392** 45
- [87] Zhang F, Jung J, Fiete G A, Niu Q and MacDonald A H 2011 *Phys. Rev. Lett.* **106** 156801
- [88] Ando T, Nakanishi T and Saito R 1998 *J. Phys. Soc. Japan* **67** 2857
- [89] Dresselhaus G 1974 *Phys. Rev. B* **10** 3602
- [90] Nakao K 1976 *J. Phys. Soc. Japan* **40** 761
- [91] Inoue M 1962 *J. Phys. Soc. Japan* **17** 808
- [92] Gupta O P and Wallace P R 1972 *Phys. Status. Solidi. b* **54** 53
- [93] Lifshitz L M 1960 *Zh. Exp. Teor. Fiz.* **38** 1565
- [94] Lifshitz L M 1960 *Sov. Phys.—JETP* **11** 1130
- [95] Mikitik G P and Sharlai Y 2008 *Phys. Rev. B* **77** 113407
- [96] Wallace P R 1947 *Phys. Rev.* **71** 622
- [97] Johnson J G and Dresselhaus G 1973 *Phys. Rev. B* **7** 2275
- [98] Sasaki K, Murakami S and Saito R 2006 *Appl. Phys. Lett.* **88** 113110
- [99] Peres N M R, Guinea F and Castro Neto A H 2006 *Phys. Rev. B* **73** 125411
- [100] Kane C L and Mele E J 2005 *Phys. Rev. Lett.* **95** 226801
- [101] Min H, Hill J E, Sinitsyn N A, Sahu B R, Kleinman L and MacDonald A H 2006 *Phys. Rev. B* **74** 165310
- [102] Huertas-Hernando D, Guinea F and Brataas A 2006 *Phys. Rev. B* **74** 155426
- [103] Yao Y, Ye F, Qi X-L, Zhang S-C and Fang Z 2007 *Phys. Rev. B* **75** 041401(R)
- [104] Boettger J C and Trickey S B 2007 *Phys. Rev. B* **75** 121402(R)
- [105] Gmitra M, Konschuh S, Ertler C, Ambrosch-Draxl C and Fabian J 2009 *Phys. Rev. B* **80** 235431
- [106] van Gelderen R and Morais Smith C 2010 *Phys. Rev. B* **81** 125435
- [107] Guinea F 2010 *New J. Phys.* **12** 083063
- [108] Liu H-W, Xie X C and Sun Q-F 2010 arXiv:1004.0881
- [109] McCann E and Koshino M 2010 *Phys. Rev. B* **81** 241409(R)
- [110] Konschuh S, Gmitra M, Kochan D and Fabian J 2012 *Phys. Rev. B* **85** 115423
- [111] Cortijo A, Grushin A G and Vozmediano M A H 2010 *Phys. Rev. B* **82** 195438
- [112] Prada E, San-Jose P, Brey L and Fertig H A 2011 *Solid State Commun.* **151** 1075
- [113] Bychkov Y A and Rashba E I 1984 *J. Phys. C: Solid State Phys.* **17** 6039
- [114] Rashba E I 2009 *Phys. Rev. B* **79** 161409
- [115] Rakytá P, Kormanyos A and Cserti J 2010 *Phys. Rev. B* **82** 113405
- [116] Qiao Z, Tse W-K, Jiang H, Yao Y and Niu Q 2011 *Phys. Rev. Lett.* **107** 256801

- [116] Mireles F and Schliemann J 2012 *New J. Phys.* **14** 093026
- [117] Landau L D 1930 *Z. Phys.* **64** 629
- [118] von Klitzing K, Dorda G and Pepper M 1980 *Phys. Rev. Lett.* **45** 494
- [119] Prange R E and Girvin S M (ed) 1986 *The Quantum Hall Effect* (New York: Springer)
- [120] MacDonald A H (ed) 1989 *Quantum Hall Effect: A Perspective* (Boston MA: Kluwer)
- [121] McClure J W 1956 *Phys. Rev.* **104** 666
- [122] Zheng Y and Ando T 2002 *Phys. Rev. B* **65** 245420
- [123] Gusynin V P and Sharapov S G 2005 *Phys. Rev. Lett.* **95** 146801
- [124] Herbut I F 2007 *Phys. Rev. B* **75** 165411
- [125] Milton Pereira J Jr, Peeters F M and Vasilopoulos P 2007 *Phys. Rev. B* **76** 115419
- [126] Mucha-Kruczyński M, McCann E and Fal'ko V I 2009 *Solid State Commun.* **149** 1111
- [127] Nakamura M, Castro E V and Dora B 2009 *Phys. Rev. Lett.* **103** 266804
- [128] Zhang L M, Fogler M M and Arovas D P 2011 *Phys. Rev. B* **84** 075451
- [129] Mak K F, Lui C H, Shan J and Heinz T F 2009 *Phys. Rev. Lett.* **102** 256405
- [130] Zhang Y, Tang T-T, Girit C, Hao Z, Martin M C, Zettl A, Crommie M F, Shen Y R and Wang F 2009 *Nature* **459** 820
- [131] Henriksen E A and Eisenstein J P 2010 *Phys. Rev. B* **82** 041412
- [132] Young A F, Dean C R, Meric I, Sorgenfrei S, Ren H, Watanabe K, Taniguchi T, Hone J, Shepard K L and Kim P 2012 *Phys. Rev. B* **85** 235458
- [133] Deshpande A, Bao W, Zhao Z, Lau C N and LeRoy B J 2009 *Appl. Phys. Lett.* **95** 243502
- [134] Szafrank B N, Schall D, Otto M, Neumaier D and Kurz H 2010 *Appl. Phys. Lett.* **96** 112103
- [135] Zou K and Zhu J 2010 *Phys. Rev. B* **82** 081407(R)
- [136] Miyazaki H, Tsukagoshi K, Kanda A, Otani M and Okada S 2010 *Nano Lett.* **10** 3888
- [137] Jing L, Velasco J Jr, Kratz P, Liu G, Bao W Z, Bockrath M and Lau C N 2010 *Nano Lett.* **10** 4000
- [138] Taychatanapat T and Jarillo-Herrero P 2010 *Phys. Rev. Lett.* **105** 166601
- [139] Yan J and Fuhrer M S 2010 *Nano Lett.* **10** 4521
- [140] Li J, Martin I, Büttiker M and Morpurgo A F 2011 *Nature Phys.* **7** 38
- [141] Castro E V, Lopez-Sancho M P and Vozmediano M A H 2010 *Phys. Rev. Lett.* **104** 036802
- [142] Rossi E and Das Sarma S 2011 *Phys. Rev. Lett.* **107** 155502
- [143] Abergel D S L, Min H K, Hwang E H and Das Sarma S 2012 *Phys. Rev. B* **85** 045411
- [144] Trushin M 2012 *Europhys. Lett.* **98** 47007
- [145] Fogler M M and McCann E 2010 *Phys. Rev. B* **82** 197401
- [146] Castro E V, Novoselov K S, Morozov S V, Peres N M R, Lopes dos Santos J M B, Nilsson J, Guinea F, Geim A K and Castro Neto A H 2010 *J. Phys.: Condens. Matter* **22** 175503
- [147] Koshino M and McCann E 2009 *Phys. Rev. B* **79** 125443
- [148] Falkovsky L A 2009 *Phys. Rev. B* **80** 113413
- [149] Nilsson J and Castro Neto A H 2007 *Phys. Rev. Lett.* **98** 126801
- [150] Castro E V, Peres N M R and Lopes dos Santos J M B 2007 *Phys. Status Solidi b* **244** 2311
- [151] Mkhitarian V V and Raikh M E 2008 *Phys. Rev. B* **78** 195409
- [152] Abergel D S L, Hwang E H and Das Sarma S 2011 *Phys. Rev. B* **83** 085429
- [153] Min H, Abergel D S L, Hwang E H and Das Sarma S 2011 *Phys. Rev. B* **84** 041406(R)
- [154] Abergel D S L, Min H, Hwang E H and Das Sarma S 2011 *Phys. Rev. B* **84** 195423
- [155] Rutter G M, Jung S, Klimov N N, Newell D B, Zhitenev N B and Strosio J A 2011 *Nature Phys.* **7** 649
- [156] Avetisyan A A, Partoens B and Peeters F M 2009 *Phys. Rev. B* **79** 035421
- [157] Avetisyan A A, Partoens B and Peeters F M 2009 *Phys. Rev. B* **80** 195401
- [158] Koshino M 2010 *Phys. Rev. B* **81** 125304
- [159] Gorbachev R V, Tikhonenko F V, Mayorov A S, Horsell D W and Savchenko A K 2007 *Phys. Rev. Lett.* **98** 176805
- [160] Morozov S V, Novoselov K S, Katsnelson M I, Schedin F, Elias D C, Jaszczak J A and Geim A K 2008 *Phys. Rev. Lett.* **100** 016602
- [161] Feldman B E, Martin J and Yacoby A 2009 *Nature Phys.* **5** 889
- [162] Xiao S, Chen J-H, Adam S, Williams E D and Fuhrer M S 2010 *Phys. Rev. B* **82** 041406
- [163] Koshino M and Ando T 2006 *Phys. Rev. B* **73** 245403
- [164] Nilsson J, Castro Neto A H, Guinea F and Peres N M R 2006 *Phys. Rev. Lett.* **97** 266801
- [165] Katsnelson M I 2006 *Eur. Phys. J. B* **52** 151
- [166] Katsnelson M I 2007 *Phys. Rev. B* **76** 073411
- [167] Cserti J 2007 *Phys. Rev. B* **75** 033405
- [168] Snyman I and Beenakker C W J 2007 *Phys. Rev. B* **75** 045322
- [169] Cserti J, Csordas A and David G 2007 *Phys. Rev. Lett.* **99** 066802
- [170] Kechedzhi K, Fal'ko V I, McCann E and Altshuler B L 2007 *Phys. Rev. Lett.* **98** 176806
- [171] Adam S and Das Sarma S 2008 *Phys. Rev. B* **77** 115436
- [172] Das Sarma S, Hwang E H and Rossi E 2010 *Phys. Rev. B* **81** 161407(R)
- [173] Trushin M, Kailasvuori J, Schliemann J and MacDonald A H 2010 *Phys. Rev. B* **82** 155308
- [174] Hwang E H and Das Sarma S 2010 *Phys. Rev. B* **82** 081409
- [175] Ferreira A, Viana-Gomes J, Nilsson J, Mucciolo E R, Peres N M R and Castro Neto A H 2011 *Phys. Rev. B* **83** 165402
- [176] Peres N M R 2010 *Rev. Mod. Phys.* **82** 2673
- [177] Das Sarma S, Adam S, Hwang E H and Rossi E 2011 *Rev. Mod. Phys.* **83** 407
- [178] Katsnelson M I, Novoselov K S and Geim A K 2006 *Nature Phys.* **2** 620
- [179] Poole C J 2010 *Solid State Commun.* **150** 632
- [180] Cheianov V V and Fal'ko V I 2006 *Phys. Rev. B* **74** 041403(R)
- [181] Nilsson J, Castro Neto A H, Guinea F and Peres N M R 2007 *Phys. Rev. B* **76** 165416
- [182] Nakanishi T, Koshino M and Ando T 2010 *Phys. Rev. B* **82** 125428
- [183] Koshino M, Nakanishi T and Ando T 2010 *Phys. Rev. B* **82** 205436
- [184] González J W, Santos H, Prada E, Brey L and Chico L 2011 *Phys. Rev. B* **83** 205402
- [185] Barbier M, Vasilopoulos P, Peeters F M and Milton Pereira J Jr 2009 *Phys. Rev. B* **79** 155402
- [186] Ramezani Masir M, Vasilopoulos P and Peeters F M 2009 *Phys. Rev. B* **79** 035409
- [187] Agrawal (Garg) N, Grover S, Ghosh S and Sharma M 2012 *J. Phys.: Condens. Matter* **24** 175003
- [188] Fiori G and Iannaccone G 2009 *IEEE Electr. Device Lett.* **30** 261
- [189] Martin I, Blanter Ya M and Morpurgo A F 2008 *Phys. Rev. Lett.* **100** 036804
- [190] Killi M, Wei T-C, Affleck I and Paramakanti A 2010 *Phys. Rev. Lett.* **104** 216406
- [191] Qiao Z, Jung J, Niu Q and MacDonald A H 2011 *Nano Lett.* **11** 3453
- [192] Zarenia M, Pereira J M Jr, Farias G A and Peeters F M 2011 *Phys. Rev. B* **84** 125451
- [193] San-Jose P, Prada E, McCann E and Schomerus H 2009 *Phys. Rev. Lett.* **102** 247204

- [194] Li X G, Zhang Z Y and Xiao D 2010 *Phys. Rev. B* **81** 195402
- [195] Xavier L J P, Pereira J M, Chaves A, Farias G A and Peeters F M 2010 *Appl. Phys. Lett.* **96** 212108
- [196] Schomerus H 2010 *Phys. Rev. B* **82** 165409
- [197] Schomerus H 2007 *Phys. Rev. B* **76** 045433
- [198] Tworzydło J, Trauzettel B, Titov M, Rycerz A and Beenakker C W J 2006 *Phys. Rev. Lett.* **96** 246802
- [199] Landauer R 1970 *Phil. Mag.* **21** 863
- [200] Buttiker M 1988 *IBM J. Res. Dev.* **32** 317
- [201] Shon N H and Ando T 1998 *J. Phys. Soc. Japan* **67** 2421
- [202] Koshino M 2009 *New J. Phys.* **11** 095010
- [203] Ando T 2011 *J. Phys. Soc. Japan* **80** 014707
- [204] Noro M, Koshino M and Ando T 2010 *J. Phys. Soc. Japan* **79** 04713
- [205] Altshuler B L, Khmelnitski D, Larkin A I and Lee P A 1980 *Phys. Rev. B* **22** 5142
- [206] Hikami S, Larkin A I and Nagaoka Y 1980 *Prog. Theor. Phys.* **63** 707
- [207] McEuen P L, Bockrath M, Cobden D H, Yoon Y-G and Louie S G 1999 *Phys. Rev. Lett.* **83** 5098
- [208] Suzuura H and Ando T 2002 *Phys. Rev. Lett.* **89** 266603
- [209] Morozov S V, Novoselov K S, Katsnelson M I, Schedin F, Ponomarenko L A, Jiang D and Geim A K 2006 *Phys. Rev. Lett.* **97** 016801
- [210] Morpurgo A F and Guinea F 2006 *Phys. Rev. Lett.* **97** 196804
- [211] McCann E, Kechedzhi K, Fal'ko V I, Suzuura H, Ando T and Altshuler B L 2006 *Phys. Rev. Lett.* **97** 146805
- [212] Kechedzhi K, McCann E, Fal'ko V I, Suzuura H, Ando T and Altshuler B L 2007 *Eur. Phys. J. Spec. Top.* **148** 39
- [213] Fal'ko V I, Kechedzhi K, McCann E, Altshuler B L, Suzuura H and Ando T 2007 *Solid State Commun.* **143** 33
- [214] Heersche H B, Jarillo-Herrero P, Oostinga J B, Vandersypen L M K and Morpurgo A F 2007 *Nature* **446** 56
- [215] Wu X, Li X, Song Z, Berger C and de Heer W A 2007 *Phys. Rev. Lett.* **98** 136801
- [216] Tikhonenko F V, Horsell D W, Gorbachev R V and Savchenko A K 2008 *Phys. Rev. Lett.* **100** 056802
- [217] Ki D-K, Jeong D, Choi J-H, Lee H-J and Park K-S 2008 *Phys. Rev. B* **78** 125409
- [218] Tikhonenko F V, Kozikov A A, Savchenko A K and Gorbachev R V 2009 *Phys. Rev. Lett.* **103** 226801
- [219] Lara-Avila S, Tzalenchuk A, Kubatkin S, Yakimova R, Janssen T J B M, Cedergren K, Bergsten T and Fal'ko V 2011 *Phys. Rev. Lett.* **107** 166602
- [220] McCann E 2009 *Physics* **2** 98
- [221] Imura K-I, Kuramoto Y and Nomura K 2009 *Phys. Rev. B* **80** 085119
- [222] Imura K-I, Kuramoto Y and Nomura K 2010 *Euro. Phys. Lett.* **89** 17009
- [223] McCann E and Fal'ko V I 2012 *Phys. Rev. Lett.* **108** 166606
- [224] Kechedzhi K, Fal'ko V I, McCann E and Altshuler B L 2007 *Phys. Rev. Lett.* **98** 176806
- [225] Koshino M 2008 *Phys. Rev. B* **78** 155411
- [226] Abergel D S L and Falko V I 2007 *Phys. Rev. B* **75** 155430
- [227] Nicol E J and Carbotte J P 2008 *Phys. Rev. B* **77** 155409
- [228] Koshino M and Ando T 2009 *Solid State Commun.* **149** 1123
- [229] Ando T and Koshino M 2009 *J. Phys. Soc. Japan* **78** 104716
- [230] Koshino M and Ando T 2008 *Phys. Rev. B* **77** 115313
- [231] McClure J W 1960 *Phys. Rev.* **119** 606
- [232] Sharma M P, Johnson L G and McClure J W 1974 *Phys. Rev. B* **9** 2467
- [233] Safran S A and DiSalvo F J 1979 *Phys. Rev. B* **20** 4889
- [234] Safran S A 1984 *Phys. Rev. B* **30** 421
- [235] Blinowski J and Rigaux C 1984 *J. Phys. (Paris)* **45** 545
- [236] Saito R and Kamimura H 1986 *Phys. Rev. B* **33** 7218
- [237] Koshino M and Ando T 2007 *Phys. Rev. B* **76** 085425
- [238] Nakamura M and Hirasawa L 2008 *Phys. Rev. B* **77** 045429
- [239] Koshino M and Ando T 2007 *Phys. Rev. B* **75** 235333
- [240] Fukuyama H 2007 *J. Phys. Soc. Japan* **76** 043711
- [241] Nakamura M 2007 *Phys. Rev. B* **76** 113301
- [242] Ghosal A, Goswami P and Chakravarty S 2007 *Phys. Rev. B* **75** 115123
- [243] Koshino M and Ando T 2010 *Phys. Rev. B* **81** 195431
- [244] Koshino M 2011 *Phys. Rev. B* **84** 125427
- [245] Suzuura H and Ando T 2002 *Phys. Rev. B* **65** 235412
- [246] Nanda B R K and Satpathy S 2009 *Phys. Rev. B* **80** 165430
- [247] Choi S-M, Jhi S-H and Son Y-W 2010 *Nano Lett.* **10** 3486
- [248] Verberck B, Partoens B, Peeters F M and Trauzettel B 2012 *Phys. Rev. B* **85** 125403
- [249] Mucha-Kruczyński M, Aleiner I L and Fal'ko V I 2011 *Phys. Rev. B* **84** 041404
- [250] Son Y-W, Choi S-M, Hong Y P, Woo S and Jhi S-H 2011 *Phys. Rev. B* **84** 155410
- [251] Mariani E, Pearce A J and von Oppen F 2012 *Phys. Rev. B* **86** 165448
- [252] Gradinar D A, Schomerus H and Fal'ko V I 2012 *Phys. Rev. B* **85** 165429
- [253] Vafeek O and Yang K 2010 *Phys. Rev. B* **81** 041401(R)
- [254] Lemonik Y, Aleiner I L, Toke C and Fal'ko V I 2010 *Phys. Rev. B* **82** 201408(R)
- [255] Throckmorton R E and Vafeek O 2012 *Phys. Rev. B* **86** 115447
- [256] Lemonik Y, Aleiner I L and Fal'ko V I 2012 *Phys. Rev. B* **85** 245451
- [257] Reich S and Thomsen C 2004 *Phil. Trans. R. Soc. A* **362** 2271
- [258] Ferrari A C *et al* 2006 *Phys. Rev. Lett.* **97** 187401
- [259] Ferrari A C 2007 *Solid State Commun.* **143** 47
- [260] Malard L M, Pimenta M A, Dresselhaus G and Dresselhaus M S 2009 *Phys. Rep.* **473** 51
- [261] Grüneis A, Saito R, Kimura T, Cançado L G, Pimenta M A, Jorio A, Souza Filho A G, Dresselhaus G and Dresselhaus M S 2002 *Phys. Rev. B* **65** 155405
- [262] Dubay O and Kresse G 2003 *Phys. Rev. B* **67** 035401
- [263] Maultzsch J, Reich S, Thomsen C, Reuquardt H and Ordejón P 2004 *Phys. Rev. Lett.* **92** 075501
- [264] Wirtz L and Rubio A 2004 *Solid State Commun.* **131** 141
- [265] Mounet N and Marzari N 2005 *Phys. Rev. B* **71** 205214
- [266] Kohn W 1959 *Phys. Rev. Lett.* **2** 393
- [267] Piscanec S, Lazzeri M, Mauri F, Ferrari A C and Robertson J 2004 *Phys. Rev. Lett.* **93** 185503
- [268] Lazzeri M, Piscanec S, Mauri F, Ferrari A C and Robertson J 2006 *Phys. Rev. B* **73** 155426
- [269] Ando T 2006 *J. Phys. Soc. Japan* **75** 124701
- [270] Castro Neto A H and Guinea F 2007 *Phys. Rev. B* **75** 045404
- [271] Pisana S, Lazzeri M, Casiraghi C, Novoselov K S, Geim A K, Ferrari A C and Mauri F 2007 *Nature Mater.* **6** 198
- [272] Yan J, Zhang Y, Kim P and Pinczuk A 2007 *Phys. Rev. Lett.* **98** 166802
- [273] Yan J, Henriksen E A, Kim P and Pinczuk A 2008 *Phys. Rev. Lett.* **101** 136804
- [274] Malard L M, Elias D C, Alves E S and Pimenta M A 2008 *Phys. Rev. Lett.* **101** 257401
- [275] Yan J, Villarsen T, Henriksen E A, Kim P and Pinczuk A 2009 *Phys. Rev. B* **80** 241417
- [276] Bruna M and Borini S 2010 *Phys. Rev. B* **81** 125421
- [277] Garcia J M *et al* 2010 *Solid State Commun.* **150** 809
- [278] Tan P H *et al* 2012 *Nature Mater.* **11** 294
- [279] Lui C H, Malard L M, Kim S, Lantz G, Laverge F E, Saito R and Heinz T F 2012 *Nano Lett.* **12** 5539
- [280] Kuzmenko A B, Benfatto L, Cappelluti E, Crassee I, van der Marel D, Blake P, Novoselov K S and Geim A K 2009 *Phys. Rev. Lett.* **103** 116804
- [281] Tang T-T *et al* 2010 *Nature Nanotechnol.* **5** 32
- [282] Yan J-A, Ruan W Y and Chou M Y 2008 *Phys. Rev. B* **77** 125401
- [283] Saha S K, Waghmare U V, Krishnamurthy H R and Sood A K 2008 *Phys. Rev. B* **78** 165421
- [284] Jiang J-W, Tang H, Wang B-S and Su Z-B 2008 *Phys. Rev. B* **77** 235421

- [285] Michel K H and Verberck B 2008 *Phys. Rev. B* **78** 085424
- [286] Kitipornchai S, He X Q and Liew K M 2005 *Phys. Rev. B* **72** 075443
- [287] Ando T 2007 *J. Phys. Soc. Japan* **76** 104711
- [288] Ando T and Koshino M 2009 *J. Phys. Soc. Japan* **78** 034709
- [289] Gava P, Lazzeri M, Saitta A M and Mauri F 2009 *Phys. Rev. B* **80** 155422
- [290] Mucha-Kruczyński M, Kashuba O and Fal'ko V I 2010 *Phys. Rev. B* **82** 045405
- [291] Ishikawa K and Ando T 2006 *J. Phys. Soc. Japan* **75** 084713
- [292] Wang X F and Chakraborty T 2007 *Phys. Rev. B* **75** 041404(R)
- [293] Stauber T, Peres N M R, Guinea F and Castro Neto A H 2007 *Phys. Rev. B* **75** 115425
- [294] Kusminskiy S V, Nilsson J, Campbell D K and Castro Neto A H 2008 *Phys. Rev. Lett.* **100** 106805
- [295] Hwang E H and Das Sarma S 2008 *Phys. Rev. Lett.* **101** 156802
- [296] Kusminskiy S V, Campbell D K and Castro Neto A H 2009 *Europhys. Lett.* **85** 58005
- [297] Borghi G, Polini M, Asgari R and MacDonald A H 2009 *Phys. Rev. B* **80** 241402
- [298] Borghi G, Polini M, Asgari R and MacDonald A H 2010 *Phys. Rev. B* **82** 155403
- [299] Sensarma R, Hwang E H and Das Sarma S 2010 *Phys. Rev. B* **82** 195428
- [300] Gamayun O V 2011 *Phys. Rev. B* **84** 085112
- [301] Castro E V, Peres N M R, Stauber T and Silva N A P 2008 *Phys. Rev. Lett.* **100** 186803
- [302] Dillenschneider R and Han J H 2008 *Phys. Rev. B* **78** 045401
- [303] Sahu B, Min H, MacDonald A H and Banerjee S K 2008 *Phys. Rev. B* **78** 045404
- [304] Park C-H and Louie S G 2010 *Nano Lett.* **10** 426
- [305] Wang X-F and Chakraborty T 2010 *Phys. Rev. B* **81** 081402
- [306] Cortijo A, Oroszlany L and Schomerus H 2010 *Phys. Rev. B* **81** 235422
- [307] Toke C and Fal'ko V I 2011 *Phys. Rev. B* **83** 115455
- [308] Nilsson J, Castro Neto A H, Peres N M R and Guinea F 2006 *Phys. Rev. B* **73** 214418
- [309] Vafeek O 2010 *Phys. Rev. B* **82** 205106
- [310] Zhang F, Min H, Polini M and MacDonald A H 2010 *Phys. Rev. B* **81** 041402(R)
- [311] Jung J, Zhang F and MacDonald A H 2011 *Phys. Rev. B* **83** 115408
- [312] Kharitonov M 2012 *Phys. Rev. B* **86** 195435
- [313] Nandkishore R and Levitov L 2010 *Phys. Rev. Lett.* **104** 156803
- [314] Dahal H P, Wehling T O, Bedell K S, Zhu J-X and Balatsky A V 2010 *Physica B* **405** 2241
- [315] Nandkishore R and Levitov L arXiv:1002.1966 unpublished
- [316] Nandkishore R and Levitov L 2010 *Phys. Rev. B* **82** 115124
- [317] Sun K, Yao H, Fradkin E and Kivelson S A 2009 *Phys. Rev. Lett.* **103** 046811
- [318] Weitz R T, Allen M T, Feldman B E, Martin J and Yacoby A 2010 *Science* **330** 812
- [319] Martin J, Feldman B E, Weitz R T, Allen M T and Yacoby A 2010 *Phys. Rev. Lett.* **105** 256806
- [320] Mayorov A S *et al* 2011 *Science* **333** 860
- [321] Freitag F, Trbovic J, Weiss M and Schönenberger C 2012 *Phys. Rev. Lett.* **108** 076602
- [322] Velasco J Jr *et al* 2012 *Nature Nanotechnol.* **7** 156
- [323] Bao W, Velasco J Jr, Zhang F, Jing L, Standley B, Smirnov D, Bockrath M, MacDonald A H and Lau C N 2012 *Proc. Natl Acad. Sci.* **109** 10802
- [324] Veligura A, van Elferen H J, Tombros N, Maan J C, Zeitler U and van Wees B J 2012 *Phys. Rev. B* **85** 155412
- [325] Zhang F, Min H and MacDonald A H 2012 *Phys. Rev. B* **86** 155128
- [326] Nomura K and MacDonald A H 2006 *Phys. Rev. Lett.* **96** 256602
- [327] Barlas Y, Cote R, Nomura K and MacDonald A H 2008 *Phys. Rev. Lett.* **101** 097601
- [328] Shizuya K 2009 *Phys. Rev. B* **79** 165402
- [329] Abanin D A, Parameswaran S A and Sondhi S L 2009 *Phys. Rev. Lett.* **103** 076802
- [330] Gorbar E V, Gusynin V P and Miransky V A 2010 *Phys. Rev. B* **81** 155451
- [331] Gorbar E V, Gusynin V P, Jia J and Miransky V A 2011 *Phys. Rev. B* **84** 235449
- [332] van Elferen H J, Veligura A, Kurganova E V, Zeitler U, Maan J C, Tombros N, Vera-Marun I J and van Wees B J 2012 *Phys. Rev. B* **85** 115408
- [333] Zhao Y, Cadden-Zimansky P, Jiang Z and Kim P 2010 *Phys. Rev. Lett.* **104** 066801
- [334] Kim S, Lee K and Tutuc E 2011 *Phys. Rev. Lett.* **107** 016803
- [335] Du X, Shachko I, Duerr F, Luican A and Andrei E Y 2009 *Nature* **462** 192
- [336] Bolotin K I, Ghahari F, Shulman M D, Stormer H L and Kim P 2009 *Nature* **462** 196
- [337] Dean C R, Young A F, Cadden-Zimansky P, Wang L, Ren H, Watanabe K, Taniguchi T, Kim P, Hone J and Shepard K L 2011 *Nature Phys.* **7** 693
- [338] Bao W, Zhao Z, Zhang H, Liu G, Kratz P, Jing L, Velasco J Jr, Smirnov D and Lau C N 2010 *Phys. Rev. Lett.* **105** 246601
- [339] Shibata N and Nomura K 2009 *J. Phys. Soc. Japan* **78** 104708
- [340] Apalkov V M and Chakraborty T 2010 *Phys. Rev. Lett.* **105** 036801
- [341] Apalkov V M and Chakraborty T 2011 *Phys. Rev. Lett.* **107** 186803
- [342] Papic Z, Abanin D A, Barlas Y and Bhatt R N 2011 *Phys. Rev. B* **84** 241306(R)
- [343] Snizhko K, Cheianov V and Simon S H 2012 *Phys. Rev. B* **85** 201415(R)
- [344] Avouris P 2010 *Nano Lett.* **10** 4285
- [345] Andrei E Y, Li G and Du X 2012 *Rep. Prog. Phys.* **75** 056501
- [346] Yazyev O V 2010 *Rep. Prog. Phys.* **73** 056501
- [347] Pesin D and MacDonald A H 2012 *Nature Mater.* **11** 409
- [348] Beenakker C W J 2008 *Rev. Mod. Phys.* **80** 1337
- [349] Abergel D S L, Apalkov V, Berashevich J, Ziegler K and Chakraborty T 2010 *Adv. Phys.* **59** 261